

Chapter 1

Introduction

1.1 Charge Transport in Organic Semiconductors

1.1.1 Organic Semiconductors

Conductive polymers were first discovered in 1977 by Shirakawa et al^{6,7} for which they were awarded the Nobel prize in Chemistry. Recently these materials have become ubiquitous in many technologies, such as in organic photovoltaic cells⁸, organic field-effect transistors (OFET)⁹ and organic light-emitting diodes (OLED)¹⁰. While the other two technologies lag behind their inorganic counterparts, uptake of OLED screens is becoming ubiquitous -especially in the smartphone and television market due to their flexibility, better colour representation and lower energy consumption than standard backlit LCD displays. OLEDs have also found uses in lighting with their efficiency rivalling that of fluorescent tubes^{11,12}. Although, industry has made large strides in fabricating and using these materials the exact nature of the charge transport is still poorly understood. Traditional theories (such as hopping and band transport) aren't applicable to many relevant materials^{13–17} as charge transfer dynamics lies in an intermediate region where the polaron is neither fully localised or delocalised. This is due to crystals typically being formed of organic molecules weakly held together by Van der Waals (VDW) forces rather than strong covalent bonds. This allows molecules to fluctuate about their lattice sites and introduces a disorder that doesn't appear in inorganic crystals.

In order to properly quantify the performance of organic semiconductors a key prop-

erty is the charge carrier mobility. Typically, charge carrier mobilities in ‘good’ organic semiconductors (OSCs) fall between $1\text{-}10 \text{ cm}^2\text{V}^{-1}\text{s}^{-1}$ ¹⁸. Though higher mobilities, in pure crystals such as Rubrene, have been recorded in the range $15\text{-}20+ \text{ cm}^2\text{V}^{-1}\text{s}^{-1}$ ^{19,20}. This is beyond the range of hopping model validity ($\sim 1 \text{ cm}^2\text{V}^{-1}\text{s}^{-1}$) and below that of band theory ($> 50 \text{ cm}^2\text{V}^{-1}\text{s}^{-1}$)¹⁷. In this intermediate regime the charge carriers are typically not completely delocalised at the valence band edges (band regime) or localised to a single site/molecule (hopping regime) but delocalised over a few/tens of molecules²¹. Without any analytic approaches currently being valid in this regime many atomistic computational approaches have been developed to investigate the underlying charge transport mechanisms²².

1.2 Atomistic Simulations of Nonadiabatic Processes

In simulating processes involving electronic transfers a key approximation used in conventional molecular dynamics (MD) breaks down. That is the Born-Oppenheimer or adiabatic approximation²³. This approximation, relied upon for almost a century²⁴, hinges on the fact that nuclei are much more massive than electrons and are approximately stationary with respect to electron movement²⁵. This results in nuclear evolution that is governed by a single, adiabatic, potential energy surface. However, in many interesting processes, such as the proton coupled electron transfer in photosynthesis and respiration^{26–28}, non-radiative decay and photochemical processes, electronic transitions between adiabatic potential energy surfaces occur²⁹. Simulating these processes requires non-adiabatic molecular dynamics (NAMD) techniques to be developed, to correctly capture dynamical properties.

There have been many techniques proposed for use in NAMD such as the quantum classical Louiville equation³⁰, multiple spawning³¹ or nonadiabatic Bohmian dynamics³². However, two of the most popular are trajectory surface hopping³³ and mean-field approaches³⁴. This is probably due to their relative simplicity to implement, efficiency for

large systems and proven efficacy in a wide variety of situations³⁵. In these approaches the general aim is to treat as much of the system as possible with (computationally cheaper) classical mechanics. While handling all necessary parts with quantum mechanics³⁶. In Surface Hopping, Ehrenfest and Coupled-Trajectory Mixed Quantum-Classical molecular dynamics (CTMQC) one treats the nuclear subsystem classically and the electronic one quantum mechanically. The nuclei are normally propagated using a velocity verlet algorithm according to Newton's laws and electrons using a fourth order Runge Kutta algorithm according to the time-dependent Schrödinger equation. The wavefunction is normally expanded as a linear combination of adiabatic or diabatic states. The nuclei and electrons can also interact. Taking account of this interaction is where these techniques differ. No one technique is perfect, the issues for surface hopping and Ehrenfest are well documented and have been discussed in detail³⁷⁻⁴¹. CTMQC is a fairly new technique and its issues are still mostly unknown. In this document I will discuss CTMQC in depth and present results from my own implementation of it as well as presenting its drawbacks. I will also compare these results to Ehrenfest and Trajectory Surface Hopping (TSH).

1.2.1 Surface Hopping and Ehrenfest Dynamics

An important technique in the field of mixed quantum classical nonadiabatic molecular dynamics is Ehrenfest dynamics. Assuming we treat the nuclei classically the Ehrenfest equations can be rigorously derived from the electronic Schrödinger equation. This is done by assuming that the nuclei's motion is provided by a single population weighted average potential energy surface. This average is taken from the adiabatic potential energy surfaces (eigenvalues of the Hamiltonian) where weights are provided by the populations of each adiabatic state. This effective potential energy surface is shown in fig 1.1. In this way the electronic

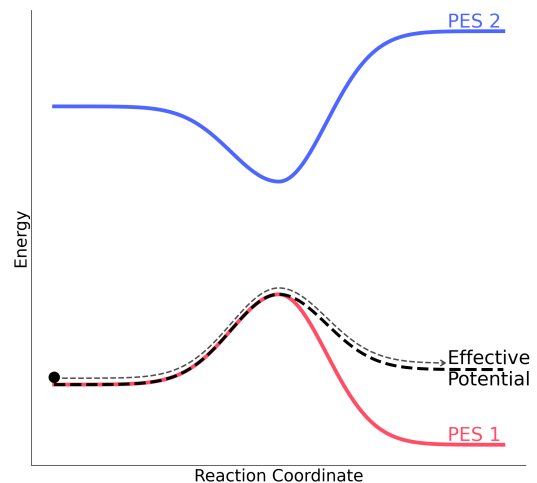


Figure 1.1: An example of a typical Ehrenfest simulation near an avoided crossing. The black lines represent the adiabatic potential energy surface due to the ground (PES 1) and excited (PES 2) state. The red line represents the population weighted average potential the nuclei travel on.

subsystem influences the propagation of the nuclei. The propagation of the forces and the electrons are controlled by equations (1.1) and (1.2).

$$F_v^{Ehren} = \sum_i^{N_{st}} |C_i|^2 \nabla_v E_i + \sum_{i,j}^{N_{st}} C_i^* C_j (E_j - E_i) \mathbf{d}_{i,j,v} \quad (1.1)$$

$$\hbar \vec{C}_m = C_m E_m - i \hbar \sum_n^{N_{st}} C_n d_{mn}^{ad} \quad (1.2)$$

In the above equations C_i is the adiabatic expansion coefficient for state i , E_m is the energy of adiabatic state m , $\mathbf{d}_{mn,v}^{ad}$ is the nonadiabatic coupling (in the adiabatic basis) between states m and n for atom v . The d_{mn}^{ad} are the nonadiabatic coupling elements expressed in the adiabatic basis. Although the Ehrenfest method has been applied with success in many systems^{42–44} it has a number of key shortcomings. Namely, its inability to capture the branching of the nuclear wavefunction as propagation occurs on only a single potential energy surface and its poor account of the decoherence of the electronic and nuclear subsystem after an avoided crossing. Ehrenfest also violates detailed balance by populating all adiabatic states evenly^{23,45}. In the limit of infinite states this results in infinite electronic temperature⁴⁶. Possibly the most popular technique in NAMD is trajectory surface hopping. In trajectory surface hopping the shape of the potential energy surface is determined by a series of discrete stochastic hops between adiabatic potential energy surfaces⁴⁵. See fig 1.2. The probability of these hops is determined by the non-adiabatic coupling between states. A swarm of trajectories are used and the probability a hop (non-adiabatic coupling) determines how many of these change state. The nuclear dynamics are dictated by the shape of the energy surface they are travelling on. This method can capture the branching of nuclear wavepacket unlike Ehrenfest. However, it still suffers from a number of issues. The original ‘fewest switches surface hopping’ proposed by John Tully suffered from bad overcoherence of the nuclear and electronic subsystems. That is the electronic and nuclear motion was coupled long after the region of high non-adiabatic coupling (crossing region). The fact that the hops are instant leads to discontinuities and methods need

to be implemented to fix these such as velocity re-scaling. Finally, perhaps the most important shortcoming is that this technique has not been derived from first principles and cannot be guaranteed to work generally. These problems have lead to a number of other techniques being developed. One of these, CTMQC, will be studied in this thesis and is the semi-classical limit of the exact factorisation of the time-dependent Schrödinger equation.

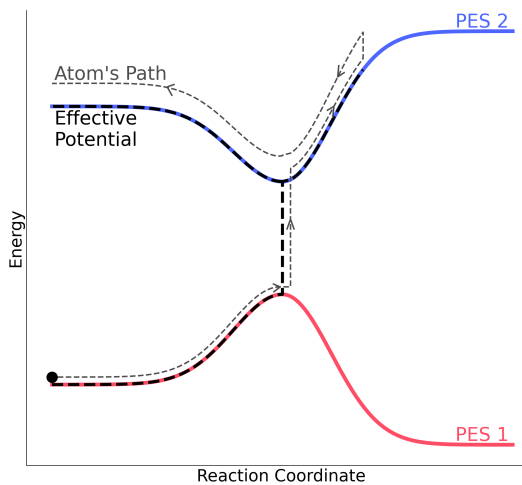


Figure 1.2: An example of a typical Surface Hopping simulation near an avoided crossing. The black lines represent the adiabatic potential energy surface due to the ground (PES 1) and excited (PES 2) state. The red line represents the discontinuous effective potential the nuclei travel on.

1.3 Exact Factorisation

Exact factorisation⁴⁷ involves separating the total molecular wavefunction into a nuclear component and electronic component. Where the electronic component is parametrically dependent on the nuclear coordinates, \mathbf{R} . This is shown below in eq (1.3) where χ is the nuclear wavefunction and Φ is the electronic one.

$$\Psi(\mathbf{R}, \mathbf{r}, t) = \Phi_{\mathbf{R}}(\mathbf{r}, t)\chi(\mathbf{R}, t) \quad (1.3)$$

In the above equation (and throughout this report) I will denote nuclear coordinates and electronic coordinates R and r respectively. The nuclear and electronic wavefunctions then obey separate, but coupled, time-dependent Schrödinger equations for spatial and temporal evolution. In this report, I will be focussing on the semi-classical limit of these equations, named Coupled-Trajectory Mixed Quantum-Classical Molecular Dynamics (CTMQC), and give results of a combination of this and the AOM method explained in section ??.

The equations for the evolution of the electronic and nuclear wavefunctions in the exact factorisation⁴⁷ are given below:

$$\hbar \frac{\delta}{\delta t} \Phi_{\mathbf{R}}(\mathbf{r}, t) = (\hat{H}_{BO} + \hat{U}_{en}[\Phi_{\mathbf{R}}, \chi] - \varepsilon(\mathbf{R}, t)) \Phi_{\mathbf{R}}(\mathbf{r}, t) \quad (1.4)$$

$$\hbar \frac{\delta}{\delta t} \chi(\mathbf{R}, t) = \left(\sum_{v=1}^{N_n} \frac{[-\hbar \nabla_v + \mathbf{A}_v(\mathbf{R}, t)]^2}{2M_v} + \varepsilon(\mathbf{R}, t) \right) \chi(\mathbf{R}, t) \quad (1.5)$$

Where \hat{H}_{BO} is the Born-Oppenheimer Hamiltonian, that is $\hat{T}_e + \hat{W}_{ee} + \hat{W}_{nn} + \hat{V}_{en}$. Where \hat{T}_e is the electronic kinetic energy operator, $\hat{W}_{ee/nn}$ is the electron-electron/nuclei-nuclei interaction and V_{en} is the electronic-nuclear potential.

The \hat{U}_{en} is an electronic-nuclear coupling operator (ENCO). This is defined as

$$\hat{U}_{en}[\Phi_{\mathbf{R}}, \chi] = \sum_{v=1}^{N_{nuc}} \frac{1}{M_v} \left[\frac{[-\hbar \nabla_v - \mathbf{A}_v(\mathbf{R}, t)]^2}{2} + \left(\frac{-\hbar \nabla_v \chi}{\chi} + \mathbf{A}_v(\mathbf{R}, t) \right) \left(-\hbar \nabla_v - \mathbf{A}_v(\mathbf{R}, t) \right) \right] \quad (1.6)$$

Where the \mathbf{A}_v is a time-dependent vector potential (TDVP), given by $\langle \Phi_{\mathbf{R}}(t) | -\hbar \nabla_v \Phi_{\mathbf{R}} \rangle_{\mathbf{r}}$ and M_v is the mass of nuclei v . Finally $\epsilon(\mathbf{R}, t)$ is a time-dependent scalar potential energy surface (TDPES), given by $\langle \Phi_{\mathbf{R}}(t) | \hat{H}_{BO} + \hat{U}_{en}^{coup} - \hbar \frac{\delta}{\delta t} | \Phi_{\mathbf{R}}(t) \rangle_{\mathbf{r}}$.

The effects of the TDPES, TDVP and the ENCO have been investigated in multiple works^{1,48–51}. The TDPES and TDVP are both responsible for the evolution of the system⁴⁸. The TDPES provides exact classical forces on the nuclei. In fact, an alternative independent-trajectory semi-classical scheme has been investigated using these exact forces¹. This found the TDPES is responsible for the splitting of the nuclear wavepacket in regions of high non-adiabaticity by taking the shape of a step function between the 2 adiabatic potentials. This is demonstrated in figure 1.3, which was adapted from an image in Agostini, 15⁴⁸.

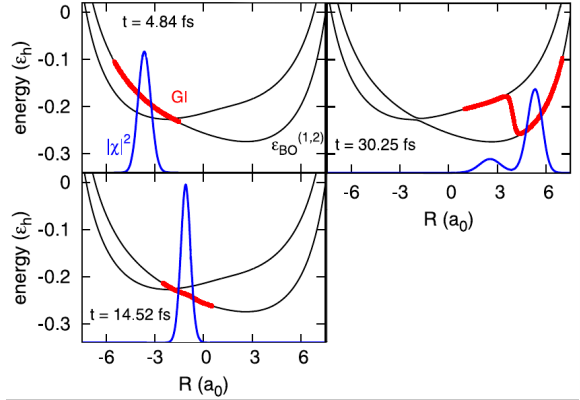


Figure 1.3: A demonstration of how the TDPES can cause the splitting of the nuclear wavepacket in non-adiabatic regions. The red line represents the TDPES and the blue is the nuclear density. Figure adapted from Agostini, 15¹

Finally the electronic-nuclear coupling operator (ENCO) is responsible for other non-adiabatic effects in the system such as electronic nonadiabatic transitions and decoherence⁴⁸.

1.4 Approximations leading to CTMQC

Starting from the exact factorisation equations, 6 approximations have been made to derive the CTMQC equations. These are discussed in detail in Ref.². In the interest of completeness I have summarised them below.

1.4.1 Classical Nuclei

Techniques that include nuclear quantum effects (NQEs); such as multiple spawning³¹, ring-polymer surface hopping⁵² and nonadiabatic Bohmian dynamics^{53,54} although extremely accurate, cannot be applied to hundreds or thousands of molecules, due to their high computational cost. Further, in many systems of interest NQEs are negligible, especially at room temperature. For this reason the classical limit of the nuclear Schrödinger equation (1.5) is taken when deriving the CTMQC equations.

1.4.2 Neglect the ENCO in the TDPES

The electron-nuclei coupling operator is omitted in the expression for the time-dependent potential energy surface. This is justified as the first term ($(-\hbar\nabla_{\mathbf{v}} - \mathbf{A}_{\mathbf{v}}(\mathbf{R}, t))^2$) contains a second order derivative which is expensive to calculate and has a negligible effect compared to the second term in the ENCO⁵⁵. However, the rest of the ENCO is equal to zero when averaged over $\Phi_{\mathbf{R}}(\mathbf{r}, t)$ so it does not contribute to the TDPES.

1.4.3 Derivative of the Adiabatic Coefficients

The derivative of the adiabatic coefficients appears in the electronic evolution equations. However, we can re-write the derivative of the adiabatic coefficients in terms of their modulus and phase:

$$\nabla_{\mathbf{v}} C_l^{(I)}(t) = \left[\underbrace{\frac{\nabla_{\mathbf{v}} |C_l^{(I)}(t)|}{|C_l^{(I)}(t)|}}_{\text{(Term 1)}} + \underbrace{\frac{i}{\hbar} \nabla_{\mathbf{v}} \gamma_l^{(I)}(t)}_{\text{(Term 2)}} \right] C_l^{(I)}(t) \quad (1.7)$$

It has been found that the first term is negligible compared to the second^{1,49,50} so it doesn't need to be calculated and we can remove it. It was also assumed that the NACVs are localised in space meaning that, after some algebra, the spatial derivative of the adiabatic coefficient can be written as:

$$\nabla_{\mathbf{v}} C_l^{(I)}(t) = \frac{i}{\hbar} \nabla_{\mathbf{v}} \gamma_l^{(I)}(t) C_l^{(I)}(t) = -\frac{i}{\hbar} \int^t dt' \nabla_{\mathbf{v}} \epsilon_l^{(I)} C_l^{(I)}(t') = -\frac{i}{\hbar} \mathbf{f}_l^{(I)} C_l^{(I)}(t) \quad (1.8)$$

Where $\epsilon_l^{(I)}$ is the energy of the l^{th} adiabatic potential energy surface for trajectory I, $C_l^{(I)}$ is the adiabatic expansion coefficient for state l and trajectory I. The $\mathbf{f}_l^{(I)}$ is the time-integrated adiabatic force (adiabatic momentum).

1.4.4 Gaussian Nuclear Wavepackets

In order to calculate the quantum momentum -the new term in CTMQC. Knowledge of the nuclear distribution is needed. However, as we treat the nuclei as point particles we need to re-construct the nuclear density from the atomic positions. This is done by smoothing out the atomic positions by placing a gaussian of width σ centered on each atomic position and combining these gaussians to produce the final nuclear density. This introduces an empirical parameter (σ) which will be discussed later in this thesis. It should be noted, the nuclei are still propagated classically, the width parameter is only used in the calculation of the quantum momentum.

1.4.5 Separating the Effects of Decoherence and NACVs

So as to not introduce any population transfer (due to the quantum momentum) when the NACV is zero a fifth approximation has been introduced. Namely the quantum momentum depends on pairs of states -l,k. This enables the separation of the ‘competing’ effects of the NACV and the Quantum Momentum.

1.5 The CTMQC equations

1.5.1 Adiabatic Basis

The equations for the propagation of the classical nuclei and the expansion coefficients in the CTMQC framework in the adiabatic basis are given below:

$$\dot{\mathbf{P}}_v^{(I)} = \underbrace{-\sum_k |C_k^{(I)}|^2 \nabla_v \epsilon_k^{(I)} - \sum_{k,l} C_l^{(I)} C_k^{*(I)} (\epsilon_k^{(I)} - \epsilon_l^{(I)})}_{\text{Ehrenfest}} - \underbrace{\sum_{l,k} |C_l^{(I)}|^2 \left(\sum_{v'=1}^{N_n} \frac{2}{\hbar M_{v'}} \mathcal{Q}_{lk,v'}^{(I)} \cdot \mathbf{f}_{l,v'}^{(I)} \right) \left[|C_k^{(I)}|^2 \mathbf{f}_{k,v}^{(I)} - \mathbf{f}_{l,v}^{(I)} \right]}_{\text{Quantum Momentum}} \quad (1.9)$$

$$\dot{C}_l^{(I)} = \underbrace{-\frac{i}{\hbar} \epsilon_l^{(I)} C_l - \sum_k C_k^{(I)} d_{lk}^{ad(I)}}_{\text{Ehrenfest}} - \underbrace{\sum_{v=1}^{N_n} \sum_k \frac{\mathcal{Q}_{lk,v}^{(I)}}{\hbar M_v} \cdot [\mathbf{f}_{k,v}^{(I)} - \mathbf{f}_{l,v}^{(I)}] |C_k^{(I)}|^2 C_l^{(I)}}_{\text{Quantum Momentum}} \quad (1.10)$$

Where the ϵ_k term is the potential energy on the k^{th} potential energy surface. C_l is the adiabatic expansion coefficient corresponding to the l^{th} state. The sum over k and l indicates a sum over all states, the (I) superscript is a replica index and the v is an atom index. M_v is the nuclear mass and $d_{lk}^{ad(I)}$ represents the non-adiabatic coupling element (in the adiabatic basis) between adiabatic states l and k . The 2 new terms in this scheme not seen in other NAMD methods are the $\mathcal{Q}_{lk,v}^{(I)}$ and the $\mathbf{f}_{k,v}^{(I)}$. These are the quantum momentum and the adiabatic momentum. The adiabatic momentum term is defined in equation (1.8) this keeps a record of the previous forces on each adiabatic state in the system. The quantum momentum term couples the trajectories together (making this a coupled-trajectory scheme). Together the history dependent force and quantum momentum are responsible for the decoherence in the ‘Quantum Momentum’ parts of the above equations³. Notably, although these equations have been derived from the exact factorisation equations separately from Ehrenfest they do contain the Ehrenfest equations within them (marked ‘Ehrenfest’). This scheme can therefore be seen as an Ehrenfest scheme with a correction that captures branching of the nuclear wavefunction and decoherence within it.

We can also see in equation (1.10) if we are in a pure adiabatic state i.e. all population on a single adiabatic state, there is no contribution from the quantum momentum part of the equations. In this scenario the evolution equations become simply Ehrenfest equations. For example, if all the population is localised on a single adiabatic state then the term $|C_k^{(I)}|^2 C_l$ is only non-zero when $l = k$. However, when $l = k$, the term $[\mathbf{f}_{k,v}^{(I)} - \mathbf{f}_{l,v}^{(I)}]$ is zero as $\mathbf{f}_{k,v}^{(I)} = \mathbf{f}_{l,v}^{(I)}$. Therefore, the quantum momentum term can be seen to only kick in when there is a mixing of adiabatic states. In the adiabatic formulation of these equations it is the adiabatic NACV $\mathbf{d}_{lk,v}^{ad,(I)}$ that is responsible for the initial mixing of the

populations from pure adiabatic states.

1.6 Calculating the Quantum Momentum

The technique for calculating the quantum momentum term is outlined in detail in the SI of min, 17⁵⁶. The original equations given in Agostini, 16² present a quantum momentum term without state indices (l,k). This, due to approximations made in the derivation of CTMQC, results in population transfer even when the non-adiabatic couplings between states are zero. Therefore, Agostini et al enforced this condition with the pair-wise state dependence on the quantum momentum. The quantum momentum is defined in equation (1.11) as:

$$\mathcal{Q}_v^{(I)} = \frac{-\hbar \nabla_v |\chi^{(I)}|}{|\chi^{(I)}|} \frac{-\hbar \nabla_v |\chi^{(I)}|^2}{2|\chi^{(I)}|^2} \quad (1.11)$$

In order to reconstruct the nuclear density, Gaussian distributions are used as in equation (1.12) below:

$$|\chi^{(I)}(t)|^2 = \frac{1}{N_{tr}} \sum_{J=1}^{N_{tr}} \prod_{v=1}^{N_n} g_{\sigma_v^{(J)}(t)} \left(\mathbf{R}_v^{(I)}(t) - \mathbf{R}_v^{(J)}(t) \right) \quad (1.12)$$

Where, N_{tr} is the number of trajectories, N_n is the number of atoms, $\sigma_v^{(J)}(t)$ is a time-dependent width parameter for each gaussian g and $\mathbf{R}_v^{(J)}$ represents the atomic position of atom v on trajectory J .

This results in a linear expression for the quantum momentum. The full details of the derivation are given in the supplementary information of Min, 17⁵⁶. The resulting linear expression for the quantum momentum is given below:

$$\mathcal{Q}_{lk,v}^{(I)} = \alpha_v^{(I)} \mathbf{R}_v^{(I)} - \mathbf{R}_{lk,v} \quad (1.13)$$

Where $\mathbf{R}_v^{(I)}$ are the nuclear coordinates on trajectory I on atom v . The $\alpha_v^{(I)}$ term is a weighted average over trajectories of the product of the gaussian's assigned to each atomic

coordinate, i.e:

$$\alpha_v^{(I)} = \sum_J^{N_{tr}} \frac{\hbar \prod_{v'} g_{\sigma_{v'}^{(J)}(t)} \left(\mathbf{R}_{v'}^{(I)}(t) - \mathbf{R}_{v'}^{(J)}(t) \right)}{2\sigma_v^{(J)}(t)^2 \sum_K^{N_{tr}} \prod_{v'} g_{\sigma_{v'}^{(K)}(t)} \left(\mathbf{R}_{v'}^{(I)}(t) - \mathbf{R}_{v'}^{(K)}(t) \right)} \quad (1.14)$$

Along with the $\mathbf{R}_{lk,v}$ term the $\alpha_v^{(I)}$ performs the job of coupling the trajectories together. The $\mathbf{R}_{lk,v}$ term also given in the SI of Min, 17⁵⁶ is defined for each Cartesian dimension as:

$$R_{lk,v} = \sum_I^{N_{tr}} R_v^{(I)}(t) \alpha_v^{(I)}(t) \frac{|C_k^{(I)}(t)|^2 |C_l^{(I)}(t)|^2 (f_{k,v}^{(I)}(t) - f_{l,v}^{(I)}(t))}{\sum_J |C_k^{(J)}(t)|^2 |C_l^{(J)}(t)|^2 (f_{k,v}^{(J)}(t) - f_{l,v}^{(J)}(t))} \quad (1.15)$$

Where the bold notation for vectors has been replaced by normal font. This means that this equation applies to each Cartesian dimension independently. Further, in this expression $R_{lk,v}$ is symmetric, $R_{lk} = R_{kl}$ meaning that $Q_{lk} = Q_{kl}$. It is also undefined on the diagonals as the denominator is 0, diagonal values are therefore set to 0. At first sight, the R_{lk} term seems to be another weighted average. However, this isn't quite the case as the denominator can be negative. This causes equation (1.15) to be very sensitive to errors in the calculation of the denominator of this fraction. Any inaccuracies can lead to the denominator approaching zero faster than the numerator causing large spikes in the quantum momentum term. This will be discussed in greater detail in the following chapters.

Chapter 2

CTMQC applied to the Tully Models

The Tully models, first proposed by John Tully in 1990⁵⁷, are a collection of simple 1 dimensional model systems. They were designed to be simple enough to obtain accurate quantum results to benchmark new nonadiabatic molecular dynamics (NAMD) methods against. Originally there were 3, 1 dimensional, 1 atom models. However, in this work an extra model has been introduced with parameters taken from Gossel, 18³. This is to allow a full comparison of my implementation of CTMQC with the literature. In this chapter my implementation of CTMQC will be tested using these model systems and by comparing my results with those in the literature.

In each of the Tully models the (diabatic) Hamiltonian is a function of nuclear positions and is a 2×2 matrix that takes the form:

$$\hat{H} = \frac{\hat{P}^2}{2M} + \begin{pmatrix} H_{11}(\mathbf{R}) & H_{12}(\mathbf{R}) \\ H_{21}(\mathbf{R}) & H_{22}(\mathbf{R}) \end{pmatrix} \quad (2.1)$$

The nuclear mass has been set to 2000 a.u.. This was set to be very close to the proton's mass of 1836 a.u. so we can expect significant quantum effects that classical theory couldn't replicate. The values of the Hamiltonian matrix elements are set to produce systems that resemble common features in a typical nonadiabatic simulation such as avoided crossings and regions of extended coupling. The parameters used in each systems' Hamiltonian where taken from Gossel, 18³ in order to compare the 2 implementations. These can be found in appendix A.

In order to propagate dynamics in the adiabatic basis we need to calculate various quantities from the hamiltonian at each timestep. These are, for Ehrenfest, the (adiabatic) nonadiabatic coupling vector ($\mathbf{d}_{lk}^{(I)}$) and the adiabatic energies ($E_l^{(I)}$). In the full CTMQC simulations we must also calculate the adiabatic momentum term $\mathbf{f}_l^{(I)}$ from the Hamiltonian. The adiabatic energies are the eigenvalues of the Hamiltonian. The adiabatic NACV can be calculated via a finite difference method and equation (2.2) below.

$$\mathbf{d}_{lk}^{(I)} = \langle \psi_l^{(I)} | \nabla \psi_k^{(I)} \rangle \quad (2.2)$$

Where $\psi_l^{(I)}$ is the adiabatic electronic basis function for adiabatic state l. This is given by the eigenvector of the Hamiltonian, on replica I, corresponding to state l. Illustrations of these 2 properties can be found below in fig 2.1 for each of the 4 models systems.

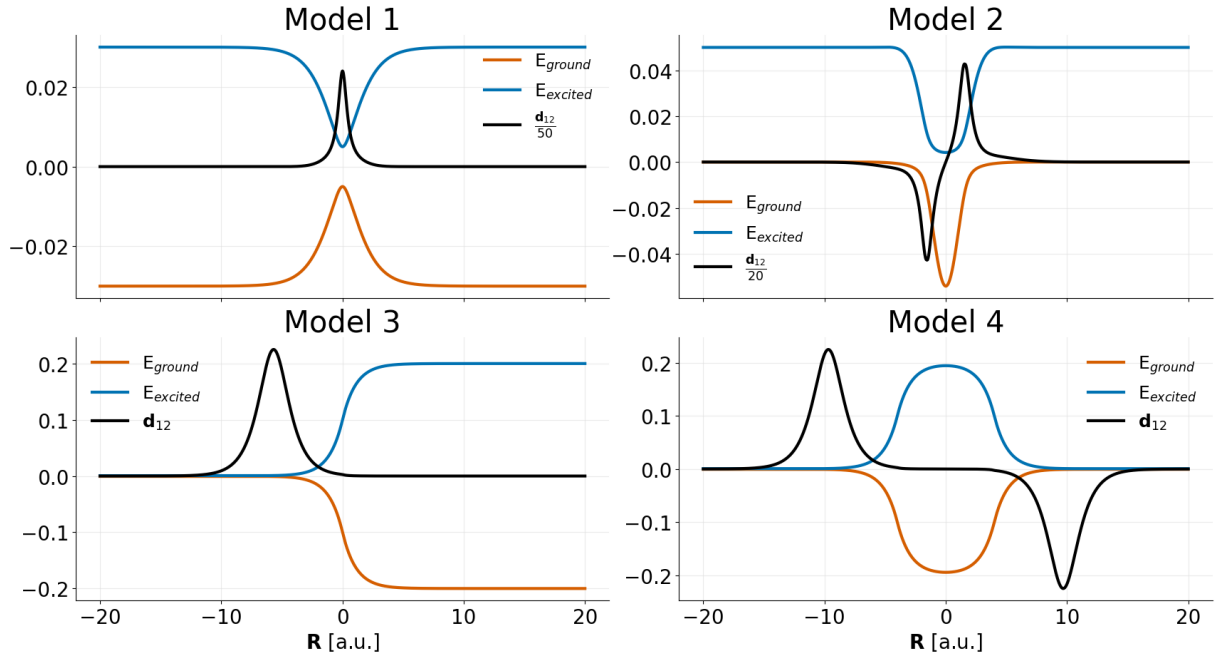


Figure 2.1: Adiabatic potential energy surfaces (orange and blue) and element 1, 2 of the nonadiabatic coupling vector (black) for the 4 model systems. For parameters see appendix A.

In order to initialise the simulations coordinates and velocities were sampled from the Wigner phase-space distribution of a gaussian nuclear wavepackets given by equation (2.3). A derivation of this can be found in appendix B. The nuclear positions/velocities were then propagated using a velocity verlet algorithm and the adiabatic expansion coefficients were propagated using a 4th order Runge-Kutta method.

$$\chi(R, 0) = \frac{1}{(\pi\mu^2)^{\frac{1}{4}}} e^{-\frac{(R-R_0)^2}{2\mu^2} + ik_0(R-R_0)} \quad (2.3)$$

The adiabatic coefficients were initialised purely on the ground state and the initial width of the nuclear wavepacket was set to $\mu = \sqrt{2}$ bohr. 2 values of initial momenta k_0 were chosen for each model, 1 low value and another higher one. Full details of all input parameters can be found in appendix A. I have implemented a serial version of CTMQC acting on Tully's toy model systems and real molecular systems using couplings derived from the analytic overlap method⁵⁸ within the software package CP2K⁵⁹ and for Tully's model systems as standalone python code. These are accessible publicly via github repositories at: github.com/95ellismle. This work will only focus on results from the CP2K implementation as we will later see this code extended and applied to systems of real Ethylene molecules.

2.1 Testing My Implementation -Ehrenfest

The motivation behind implementing CTMQC for the Tully models was to serve as a verifiable base for later extensions, such as integrating CTMQC within the fragment-orbital based (FOB)⁶⁰ framework which will be discussed in a later chapter⁷. Using such simple systems will also help to clarify how each new parameter works and make testing and debugging easier. As well as many numerical tests on individual terms in the equations, I have implemented some physical tests on the overall system dynamics. In this section, I will outline the key tests I have performed on the Ehrenfest propagation and will include the full details of the full CTMQC propagation in the following section.

In all the simulations when the Tully models are referenced they will refer to those parameters given in appendix A. Reference to a high momentum Tully model simula-

tion is a reference to that model with initial momenta being sampled from the Wigner distribution of the higher of the 2 initial momenta given in appendix A.

2.1.1 Norm Conservation

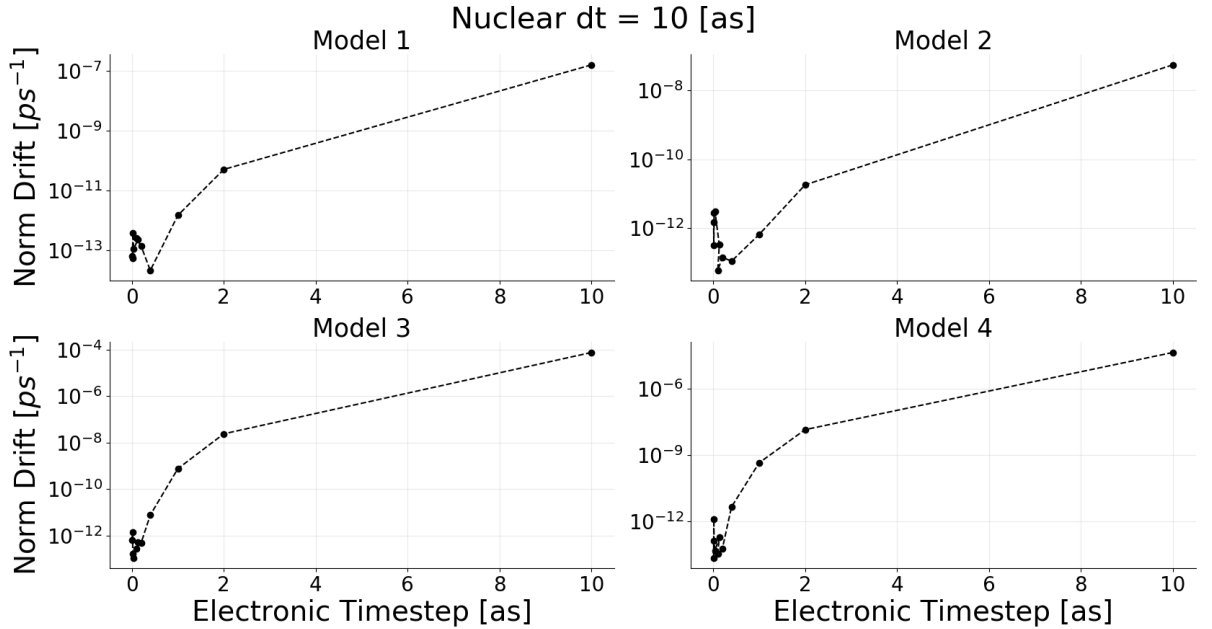


Figure 2.2: The norm conservation averaged over all replicas for Ehrenfest simulations with various electronic timesteps for each Tully model using a initial high momenta.

In appendix E, it is shown that the norm of the adiabatic expansion coefficients should be conserved throughout the simulation. To test the conservation of the norm of the expansion coefficients Ehrenfest simulations were ran with various electronic timesteps (with a constant nuclear timestep) for each of the 4 high momentum Tully models. The high momentum Tully models were chosen as they are expected to provide a worst case scenario of the norm conservation, due to populations changing more quickly leading to reduced sampling. As can be seen in figure 2.2, the norm of the wavefunction is conserved within numerical error (10^{-12}) when using a sufficiently small timestep in every Tully model.

2.1.2 Energy Conservation

Energy conservation is a very important property in most molecular dynamics simulations. In Ehrenfest of mean-field molecular dynamics nuclei are propagated on a population-weighted mean potential energy surface, e.g. $\sum_k |C_l^{(I)}(t)|^2 = E_{eff}(t)$ ⁶¹. Kinetic energy of

the classical nuclei is given by the standard formula, e.g. $\frac{1}{2}mv^2$. We can therefore write down the conserved quantity as defined below in equation (2.4):

$$\frac{dE}{dt} = \frac{d}{dt} \left[\frac{1}{2}mv^2 + \sum_k |C_l^{(I)}(t)|^2 \right] = 0 \quad (2.4)$$

As in the norm conservation checks in section ??, parameters from the high momentum cases were taken as initial conditions for simulations with various nuclear timesteps, this time holding the electronic timestep constant. The high momenta cases were chosen to show the worst case energy conservations. A linear line of best fit was then fitted to the data and the drift in the total energy (given in (2.4)) was calculated from its gradient. The results of these simulations are given in figure 2.3. In figure 2.3, we see the expected results

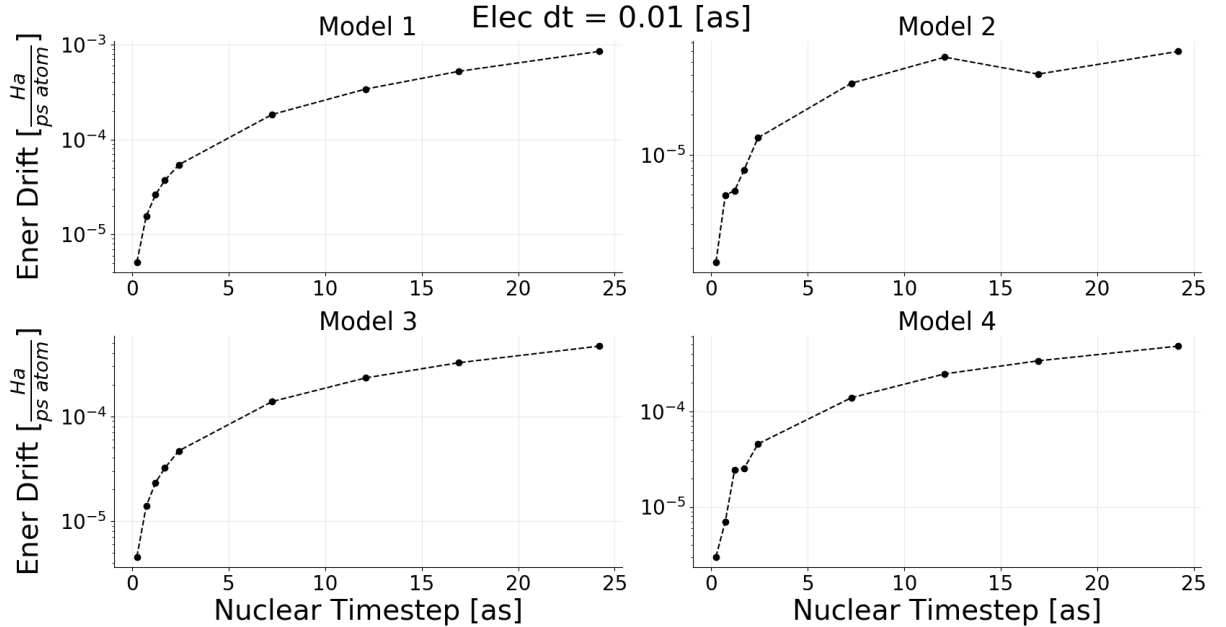


Figure 2.3: Energy conservation values for various nuclear timesteps for the high momentum case of each Tully model using Ehrenfest dynamics.

that as the nuclear timestep is decrease the drift in the total energy also decreases. This trend validates the implementation and shows that in the limit of infinitely small timestep (and infinite computer precision) perfect energy conservation would be achieved. However, fairly small nuclear timesteps are required to achieve reasonable energy conservations. This is because the system contains only 1 atom with a mass comparable to that of Hydrogen. If one needed an improved energy conservation a higher order integrator than

the velocity verlet used here may also improve results slightly.

2.1.3 Comparisons To Literature

2.1.3.1 Gossel, 18 and Agostini, 16

There have been 2 papers published applying CTMQC and Ehrenfest to the Tully models^{2,3} and both contain results for the 4 Tully models shown in fig 2.1. The results contain data on the (ground state) adiabatic populations and a coherence indicator (shown in equation (2.5)) for 16 different simulations (a low and high initial momentum simulation of Models 1, 2, 3 and 4). However, models 1 and 4 in Agostini, 16² used a different initial momentum so these have been omitted from the results in figure 2.4.

$$|\rho_{12}(t)|^2 = \frac{1}{N_{tr}} \sum_{I=1}^{N_{tr}} |C_1^{(I)}(t)|^2 |C_2^{(I)}(t)|^2 \quad (2.5)$$

In order to compare to results in the literature the same setup had to be used. In this case this meant sampling individual replicas' initial conditions (positions and momenta) from a Wigner distribution with a mean position and momenta given in appendix A. The wavefunction was initialised purely on the ground state and the same integrator was used for the nuclear and electronic propagation (velocity verlet and RK4 respectively). My results as well as the relevant data taken from Agostini, 16 and Gossel, 18^{2,3} are shown in figure 2.4 for Ehrenfest dynamics. This is equivalent to full CTMQC dynamics where the quantum momentum term is set to 0. Hence, we can test most parts of the code (i.e. Runge-Kutta propagation, velocity verlet, inputs, force calculations etc...) while ignoring the new quantum momentum and accumulated adiabatic force terms.

The results in figure 2.4 show that both the adiabatic populations and coherence indicator give exactly the same results as in the literature, within reasonable error. Any deviations of results come from either a slightly different initial sampling of positions or small errors in extracting data from the graphs in each of the papers. For example, in the case of the high initial momentum simulation of model 4 all 3 results show some

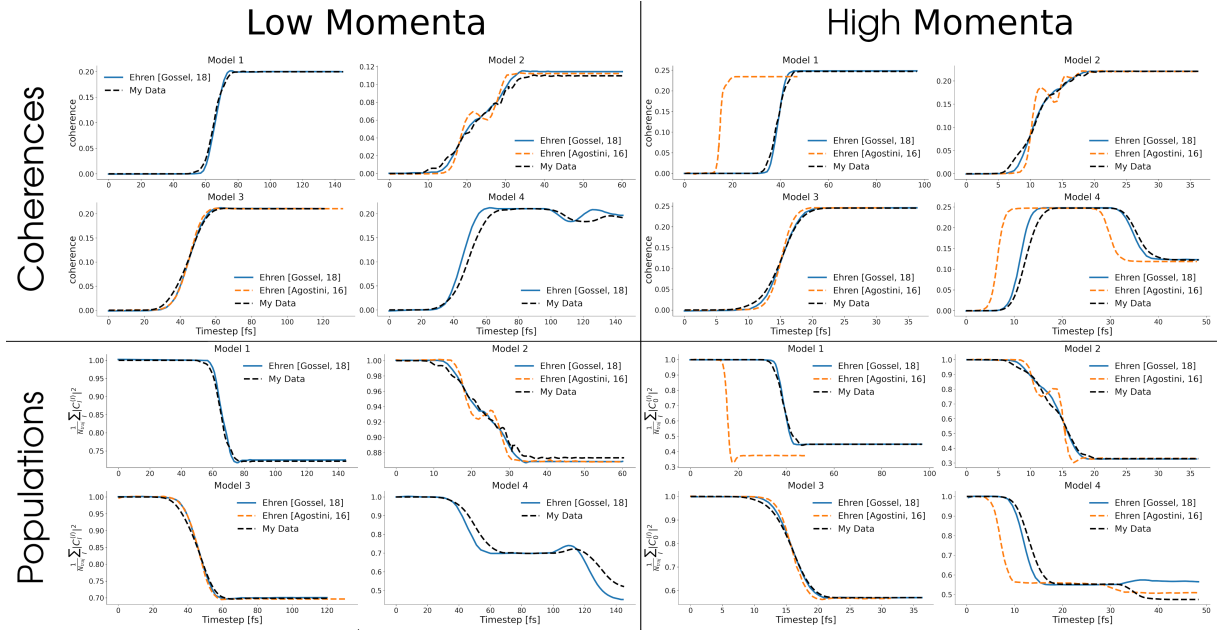


Figure 2.4: A comparison of my implementation of Ehrenfest (for 4 model Hamiltonians) and results from the literature. The black dashed lines show my data (ground state ad pops), the orange dashed lines are data from Agostini, 16² and the blue solid lines are from Gossel, 18³. The figures are labelled with their model number, whether the initial momentum was high or low and whether the populations or coherence indicator was plotted.

differences though the trend is very similar. This is true also in the Model 2 results where the Agostini, 16 populations show some transient oscillations before settling onto the same equilibrium population. This may be due to a smaller spread of positions being used in the initial sample leading to similar oscillations that aren't smoothed out in the averaging over all replicas. There are also a couple of models that start at a slightly different initial mean position in Frederica, 16 thus they hit the nonadiabatic crossing region sooner. These are model 1 and 4 for the high momentum case.

Although not all results are exactly the same, I believe the populations agree well enough within a reasonable error to serve as a confirmation of my implementation.

2.1.3.2 Subotnik, 2010

As a final confirmation of my implementation, in a Subotnik, 2010⁶², results were published for Ehrenfest simulations carried out on the 3 original Tully Models. In this work, the author presented the probabilities of the population being found transmitted through

the region of nonadiabatic coupling on the ground or excited state and the probability of being reflected on the ground or upper state. In the results below, I will show comparisons of just the transmission probability onto the ground state. That is, the population that travels on the ground state beyond the region of high nonadiabatic coupling. Other probabilities will not be shown in the interest of brevity, though they agree with the published results as well as the ground state transmission in figure 2.5. As can be seen in

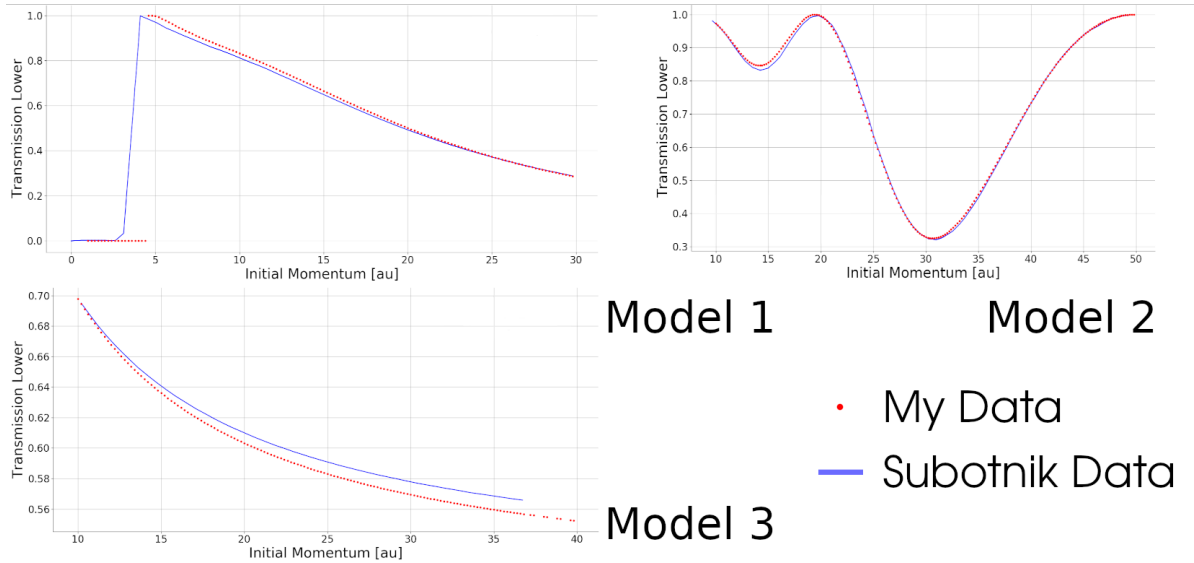


Figure 2.5: Comparison of transmission probabilities through the region of high nonadiabatic coupling on the ground state. Tully model 1 is shown in the top-left, Tully model 2 is shown in the top-right and Tully model 3 is shown in the bottom-left.

figure 2.5 my implementation of the Ehrenfest simulation code for the Tully models agrees very well with those in Subotnik, 2010⁶². The small deviation (less than 1% maximum disagreement) within each model is due to errors in retrieving data from images in original paper and possibly slightly different analysis methods.

These tests serve as a confirmation of the implementation of the Ehrenfest propagator. The full CTMQC equations can be implemented using the majority of the Ehrenfest infrastructure with extensions to account for the quantum momentum terms.

2.2 Testing my implementation -CTMQC

2.2.1 Conservation of the norm

In figure 2.6 only Model 3 shows a similar trend as in Ehrenfest for the norm conservation -i.e. a decreasing electronic timestep gives a rapidly decreasing norm drift. In models 1 and 2 we see that the norm drift doesn't get much better as we decrease the timestep and there are large error bars associated with each data point. In model 4 this is less pronounced but is still clearly affected. This is due to an instability in the current formalism of the quantum momentum term ($\mathcal{Q}_{lk,v}^{(I)}$).

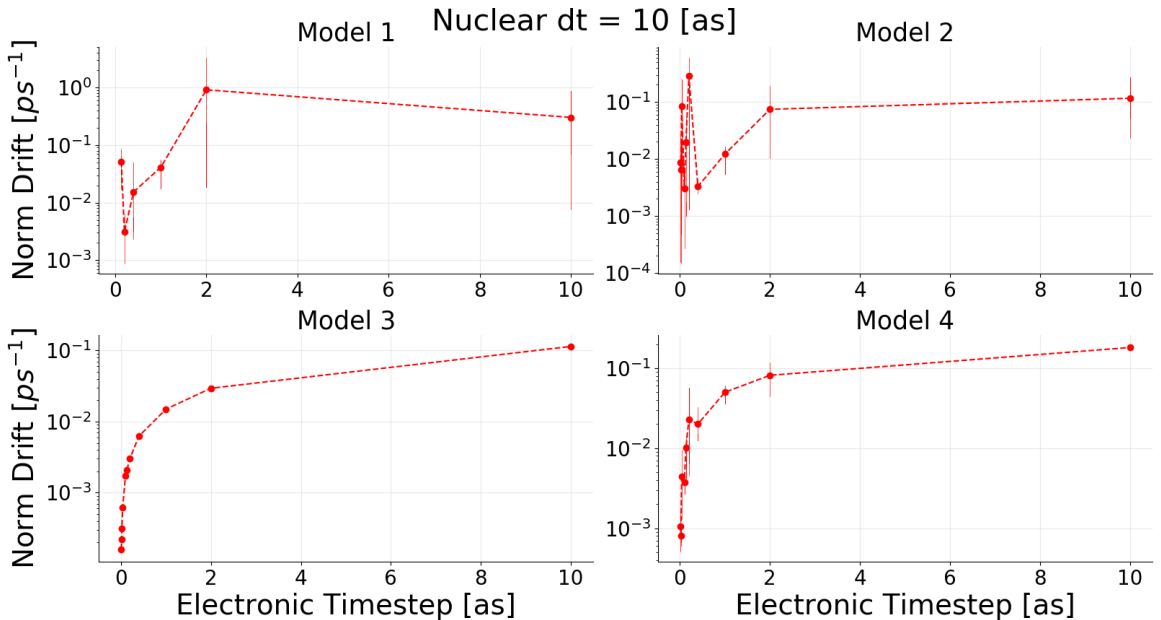


Figure 2.6: The norm conservation when using standard CTMQC as outlined in the literature for each of the Tully models. These simulations were ran with a high initial momentum. The red markers show data points and vertical bars show error bars associated with each point.

The calculation of the quantum momentum is discussed in detail in Min, 17⁵⁶ and outlined in the introduction to the thesis in section 1.6. As mentioned in that section, the denominator in the expression for $\mathbf{R}_{lk,v}$ may be positive or negative and when it switches between each it can approach zero very closely. If this denominator approaches zero more quickly than the numerator then we can see large divergence in the $\mathbf{R}_{lk,v}$ term which can lead to large norm drifts. This is highlighted in figure 2.7.

2.2.1.1 Quantum Momentum Instabilities

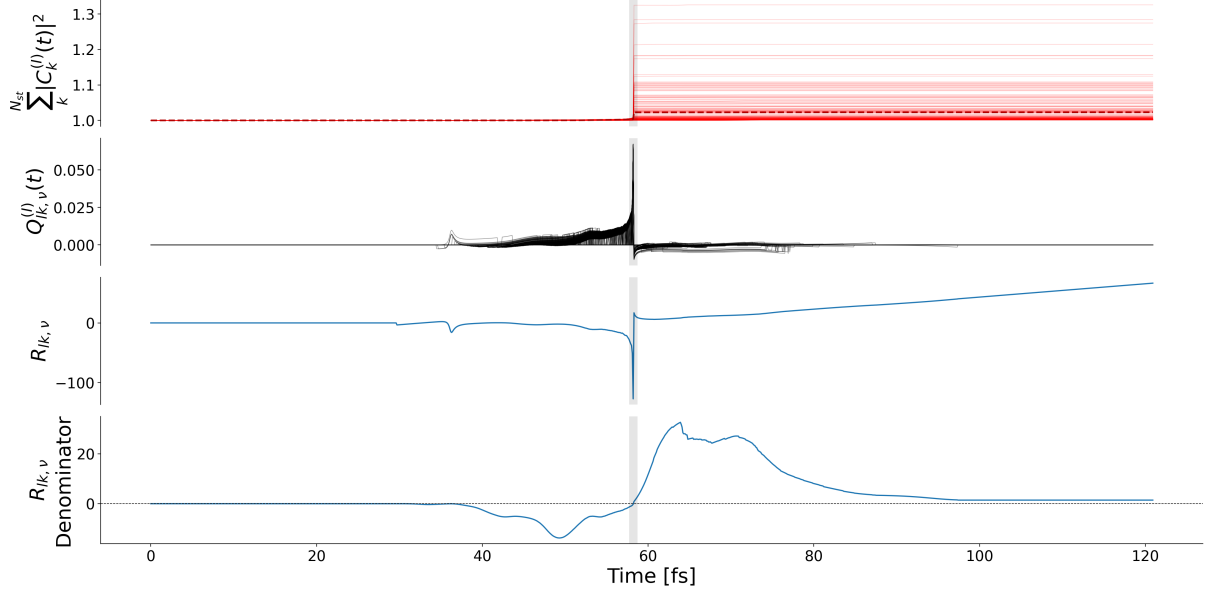


Figure 2.7: As the denominator of the $\mathbf{R}_{lk,v}$ term approaches zero (bottom panel) the full $\mathbf{R}_{lk,v}$ term (2nd to bottom panel) can approach infinity which propagates through the $\mathcal{Q}_{lk,v}^{(I)}$ term (2nd to top panel) causing discontinuities and norm drift in the populations (top panel). The grey vertical bar denotes the region the denominator approaches 0. The thin solid red lines in the top panel show the norm drift for individual replicas.

In figure 2.7, as the denominator of quantum momentum intercept (the bottom panel) approaches 0 the $\mathbf{R}_{lk,v}$ term may spike causing a discontinuity in the populations (through the quantum momentum). The reason this only occurs in Models 1, 2 and 4 is due to the fact that the difference in the adiabatic momenta terms ($\mathbf{f}_{l,v}^{(I)} - \mathbf{f}_{k,v}^{(I)}$) doesn't cross 0 in Model 3 as the time-derivative of the adiabatic energies is always either positive or negative.

In order to correct for this divergence I have investigated a number of alterations to the calculation of the quantum momentum. These depend on the detection of the spikes/divergences in the $\mathbf{R}_{lk,v}$ term and then the appropriate treatment of them. A divergence is recorded if 2 conditions are met. First is a simple threshold on the time-derivative of the intercept term, i.e. $|\frac{\delta}{\delta t} \mathbf{R}_{lk,v}| > \text{thresh}$. The second condition is a threshold on the intercept denominator i.e. $|\mathbf{R}_{denom_{lk,v}}| < \text{thresh}$. For example, if the absolute time-derivative of the $\mathbf{R}_{lk,v}$ term is larger than a value (say 5) and the bottom of the fraction in equation (1.15)

is within 0.01 of 0 then we assume the $\mathbf{R}_{lk,v}$ term is diverging and the simulation code then uses a different method of propagating the electronic coefficients. The alternative propagation methods that have been investigated are:

1. Use Ehrenfest Dynamics (set e.g. $\mathcal{Q}_{lk,v}$ term to 0).
2. Extrapolate the value of $\mathbf{R}_{lk,v}$ from values before the divergence (see appendix C.1).
3. Switch to using the alternative intercept $\mathbf{R}_{0,v}^{(I)}$ (see appendix C.2).

of these 3 methods, method 3 was the most successful in reducing the norm drift in the Tully Models as can be seen in figure 2.8.

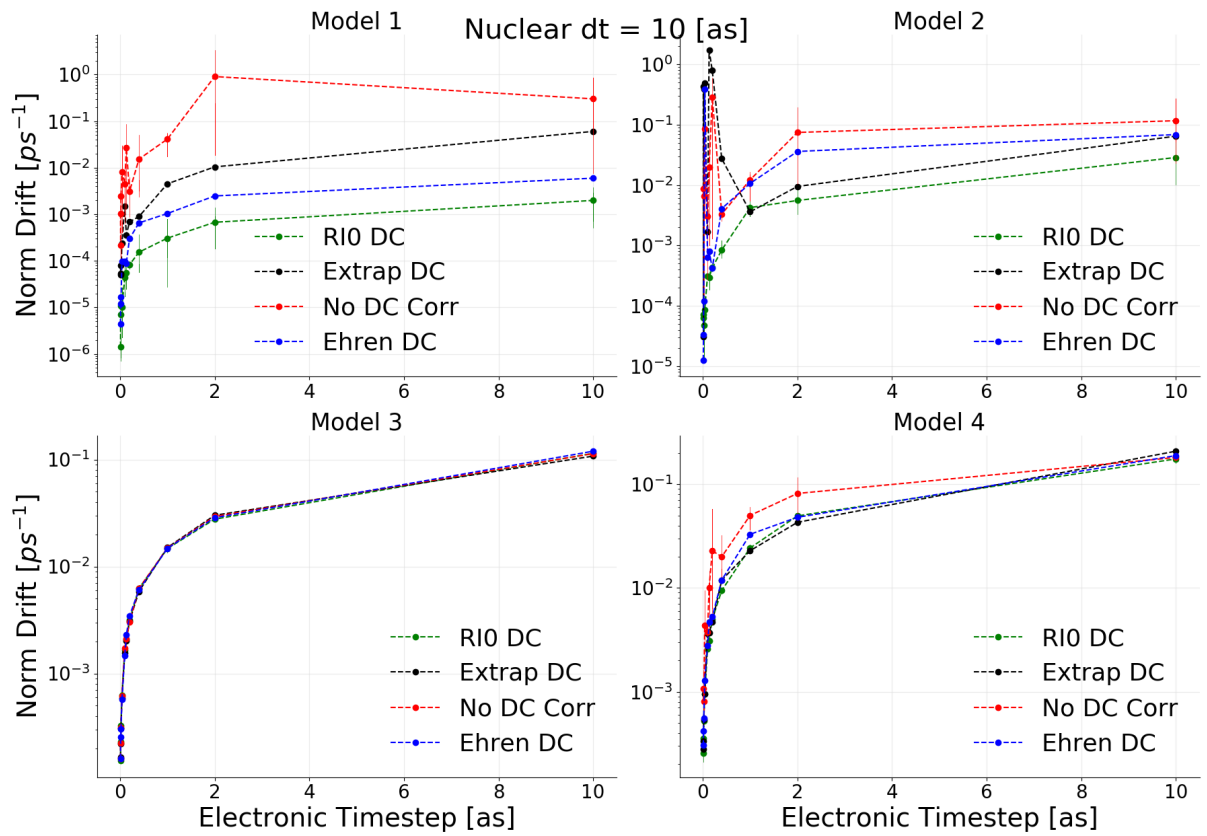


Figure 2.8: Norm conservation in CTMQC after applying a divergence correction to the $\mathbf{R}_{lk,v}$ term. RI0 refers to method 3, Extrap DC refers to method 2 and Ehren DC refers to method 1. No DC Corr shows the population norm without any corrections applied.

In figure 2.8 we see the norm drift results after the 3 $\mathbf{R}_{lk,v}$ correction methods have been applied. The red curve shows the original data (as in figure 2.6) with its large divergences in the norm drift. The green curve shows the alternative intercept method,

the blue curve shows the effect of switching to Ehrenfest during the $\mathcal{Q}_{lk,v}^{(I)}$ spikes and the black shows a method that involved extrapolating the $\mathbf{R}_{lk,v}$ value from data before the spike began. We can see clearly all 3 methods improve the norm drift, though using the alternative intercept seems to help the most. Model 3 is not affected as we do not see these divergences in the $\mathbf{R}_{lk,v}$ due to the denominator in this particular model never crossing from positive to negative (through zero). It is important to note that in each of the models with the divergence correction applied all models exhibit the expected trend of decreasing the time-step improves norm conservation. However, the norm conservation in all 4 models is still significantly higher ($\sim 7\text{-}8$ orders of magnitude) higher than that of Ehrenfest. I think this is due to the product of the adiabatic populations, $|C_l^{(I)}|^2|C_k^{(I)}|^2$, being used in the calculation of the quantum momentum which can be a more quickly varying quantity than just the adiabatic populations alone.

2.2.2 Mathematical Tests

Multiple tests of the implementation of the quantities in the equations have been implemented in the code to ensure correct outputs. A checklist of any mathematical tests is given below:

- Checking the (anti-)symmetry of the (NACV) Hamiltonian when constructed
- Comparing the adiabatic momentum term to post-production time-integrated adiabatic energies (using trapezium rule)
- Checking special case solutions when all replicas are initialised at the same position such as:
 - $\mathcal{Q}_{lk,v}^{(I)} = 0$
 - CTMQC = Ehrenfest
- Checking special cases for when $\boldsymbol{\sigma}$ is replica independent (i.e. $\boldsymbol{\sigma}^{(I)} = \boldsymbol{\sigma}$):
 - $\boldsymbol{\sigma} = \frac{\hbar}{2\sigma^2}$
 - $\mathbf{R}_{lk,v} = \mathbf{R}_v^{(I)} \frac{\hbar}{2\sigma^2}$ (Assuming the positions, $\mathbf{R}_v^{(I)}$ are also replica independent)

- If all adiabatic population is localised on a single state ($|C_l^{(I)}|^2 = [1, 0, 0, \dots, 0]$). Then we get Ehrenfest dynamics on that replica.
- Solving the static Schrödinger equation gives Rabi oscillation⁶³. See appendix D.

I have also provided 2 (more substantial) mathematical tests for the code below in the following sections.

2.2.2.1 Time Derivative of Replica-Sum of Adiabatic Populations

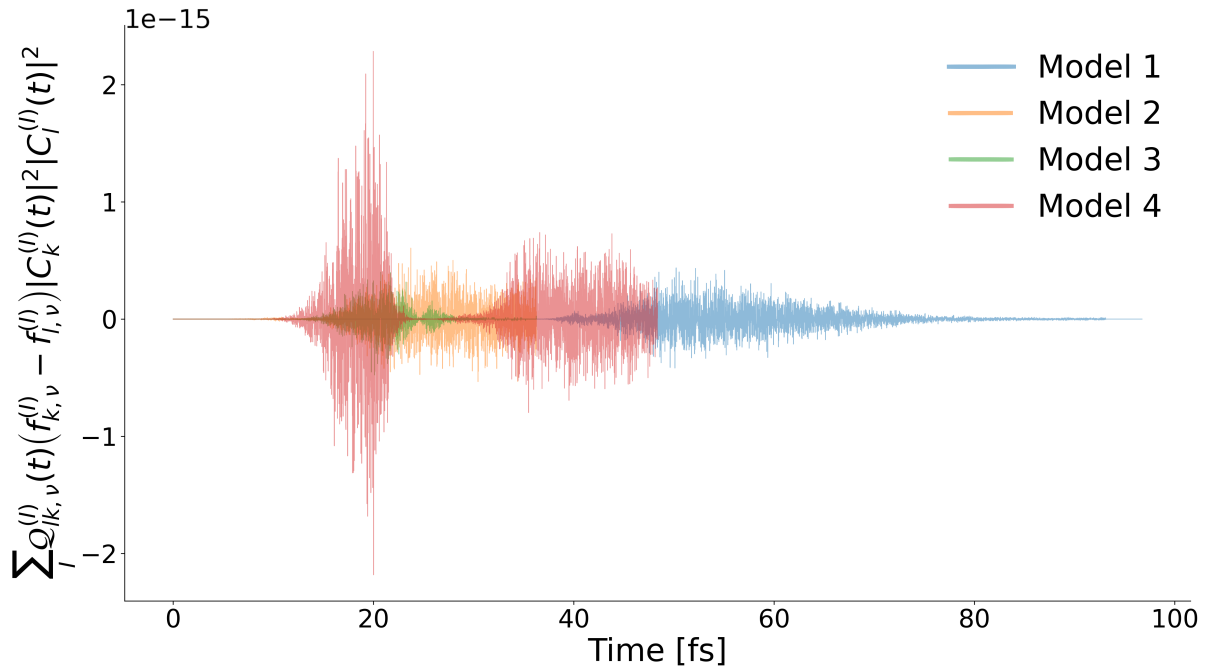


Figure 2.9: The conserved quantity given in equation (2.6). Each color represents data outputted by a simulation using a different model (specified in the legend). Each time-series is plotted with a translucent color meaning each model's data can be seen at once.

In the SI of Min, 17⁵⁶ a conservation equation (S27) is given. This is repeated below in equation (2.6)

$$\sum_I \mathcal{Q}_{lk,v}^{(I)}(t) \left(f_{k,v}^{(I)} - f_{l,v}^{(I)} \right) |C_k^{(I)}(t)|^2 |C_l^{(I)}(t)|^2 = 0 \quad \forall l, k, v \quad (2.6)$$

An example time-series of this quantity is given in figure 2.9 for each Tully model. The data used to calculate come from simulations of each of the Tully models using the parameters given in appendix A. No smoothing was used for the $\mathbf{R}_{lk,v}^{(I)}$ term. It can be

seen in this figure that the conservation quantity hovers around 0 for each model with a maximum deviation of 10^{-15} m_eHa.

2.2.2.2 $\sum_l \mathbb{X}_{qm,ll} |C_l^{(I)}|^2$

As the equations are currently formulated another numerical test validating the quantum momentum part of the propagation equations for the coefficients can be used. The CTMQC equation for the propagation of the adiabatic expansion coefficients is given in equation (1.10). The quantum momentum part of this equation is given below in equation (2.7).

$$\mathbb{X}_{qm,ll}^{(I)} = \sum_{v=1}^{N_n} \sum_k \frac{\mathcal{Q}_{lk,v}^{(I)}}{\hbar M_v} \cdot [\mathbf{f}_{k,v}^{(I)} - \mathbf{f}_{l,v}^{(I)}] |C_k^{(I)}|^2 \quad (2.7)$$

Where $\mathbb{X}_{qm,ll}^{(I)}$ is the diagonal matrix that, when multiplied with the adiabatic expansion coefficients, gives the quantum momentum contribution to the propagation of the expansion coefficients.I

We can test the construction of this matrix within the code by multiplying by the adiabatic populations and summing as shown in equation (2.8). It can be shown, assuming perfect norm conservation, that this should equal exactly 0 -due to the symmetry of the $|C_l^{(I)}|^2 |C_k^{(I)}|^2$ and the quantum momentum matrix. This is checked for every timestep during propagation.

$$\sum_l \mathbb{X}_{qm,ll}^{(I)} |C_l^{(I)}|^2 = 0 \quad (2.8)$$

2.2.3 Energy Conservation

In Agostini, 16² it is stated that the approximate potential energy is given by the same equation as in Ehrenfest, i.e. equation (2.4) a population weighted average of the potential energy surfaces. The 4 high momentum Tully models were simulated with various nuclear timesteps and a straight line of best fit was fitted to the total energy term.

As can be seen in figure 2.10 the energy conservation in CTMQC...

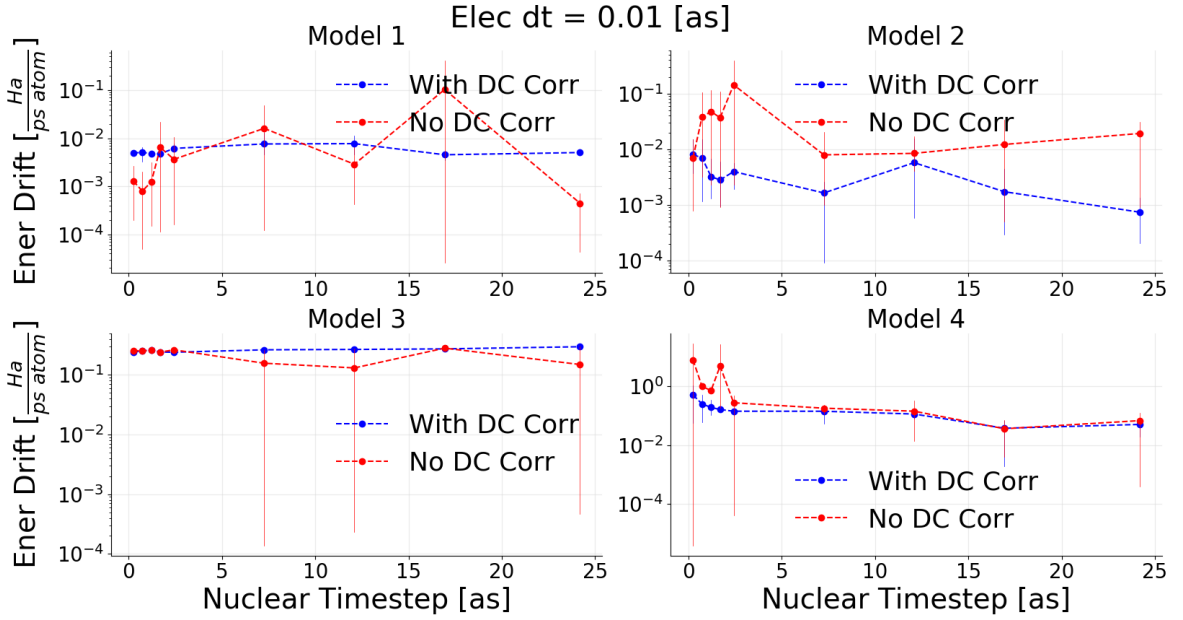


Figure 2.10: Energy drift in the 4 Tully models using the full CTMQC equations. Error bars are from multiple simulations carried out with different random sampling of the initial positions and momenta.

2.2.4 Comparisons to literature

As in section 2.1.3.1 we can compare the CTMQC results to those published before in Gossel, 18³ and Agostini, 16². These results are given in figure 2.11. This time, unlike in the Ehrenfest code, we see some discrepancies between the 3 results which cannot solely be explained as small errors from different sampling of initial positions or from errors in extracting data from graphs in the papers. We can see that the errors mainly appear in the coherence indicator, looking at the bottom row in figure 2.11 it appears that both the Agostini and Gossel results match mine (dashed black line) very closely. The largest difference is seen in model 4, high momentum where the Gossel data and mine follow a similar trend and the Agostini data follows the exact curve more closely. The reason for this is a difference in the way the adiabatic momenta terms are handled. In the Gossel paper, a method to reset the adiabatic momenta to 0 for each replica when the adiabatic populations collapse onto a pure adiabatic state (within a tolerance) is used. If this resetting is turned off then the populations in model 4 follow the Agostini results exactly. While resetting the adiabatic momenta worsens the calculation of the adiabatic populations in the model 4 high momentum simulations, it improves the convergence

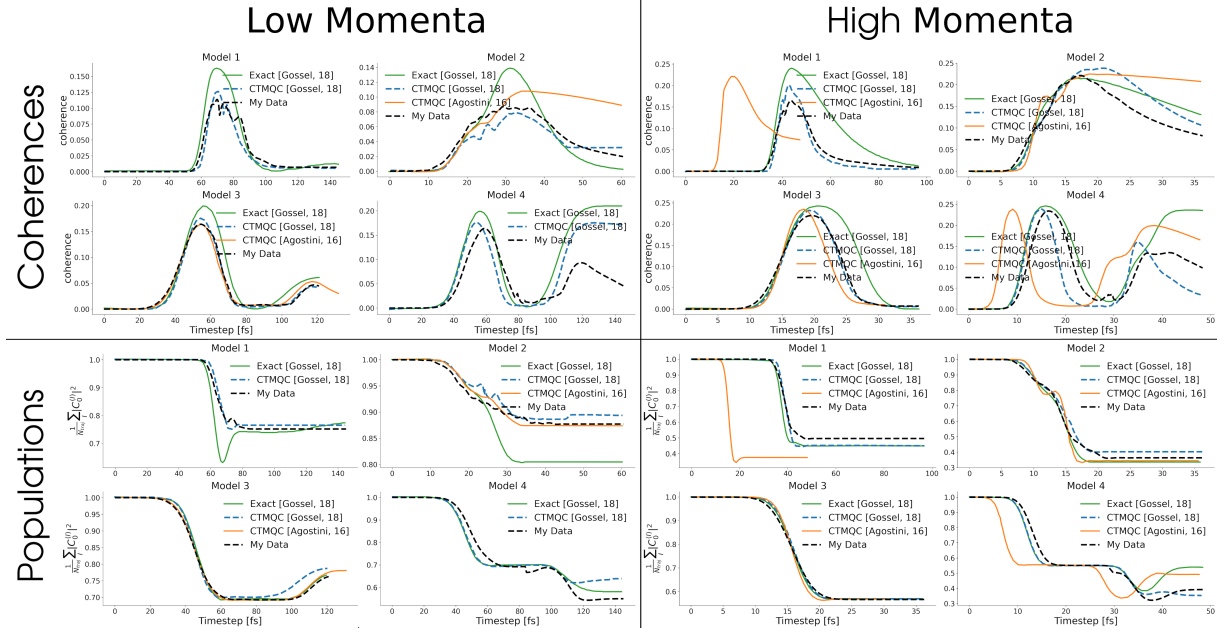


Figure 2.11: A comparison of my implementation of full CTMQC (for 4 model Hamiltonians) and results from the literature. The black dashed lines show my CTMQC data (ground state ad pops), the orange dashed lines are data from Agostini, 16² and the blue solid lines are from Gossel, 18³. The solid green line shows data from exact quantum mechanical simulations given in Gossel, 18. The figures are labelled with their model number, whether the initial momentum was high or low and whether the populations or coherence indicator was plotted.

of the coherence indicator in the model 2 simulations. I will show later how using a Other deviations in results for the populations are due to a slightly different sampling of initial positions, a different handling of divergences in the quantum momentum term and constructing the $\mathcal{Q}_{lk,v}^{(I)}$ term with a different width parameter used to construct the quantum momentum. The differences in my results and those given in the literature are on the same scale as the differences already presented in the literature and they are not large enough to invalidate my implementation. In fact many of the models agree exactly with my implementation and can be taken as a confirmation that my implementation is working.

2.3 Construction of $\mathcal{Q}_{lk,v}^{(I)}$

In order to calculate the quantum momentum the nuclear density must be constructed from the nuclei's positions. However, the nuclei are treated classically, i.e. as point particles. To approximate the nuclear density from atomic positions a normal distribution

is placed with the mean at position of each particle with a width of σ and combined . This method is outlined in the supplementary information on Min, 17⁵⁶ and introduces a new parameter which must be tuned in order to reproduce sensible results. If the width is too small the resulting nuclear density is too noisy and the quantum momentum values unreliable. If the width is too large the nuclear density is very smooth with little variation and the quantum momentum values become very small. Seeing as the quantum momentum is one of the most important factors affecting coherence between electronic states the careful selection of the σ parameter is important. This issue is not very well addressed in the literature. In this section I will show results of calculation carried out with various values of σ as well as a method for a dynamic calculation of $\sigma_v^{(I)}(t)$ on the fly. In figure 2.11 a constant value of 0.35 was used in order to best reproduce the results in Gossel, 18³.

2.3.1 Constant Values of σ

The simplest option for the calculation of $\mathcal{D}_{lk,v}^{(I)}$ is to keep the gaussian width parameter, σ , constant throughout the simulation. This also allows us to investigate the role of σ within the simulations and to determine its influence on the dynamics. To this end various simulations were carried out on the 4 Tully models with the high initial momentum. In each simulation parameters were all the same apart from the value of σ which took a value of either: 0.1, 0.2, 0.3, 0.5, 0.6, 0.75, 1 or 2 bohr. The results for these simulations are shown in figure 2.12. In this figure, we see that as the σ parameter is increased the levels of decoherence also increases. This means for larger σ values electronic populations remain in a mixed state for longer and take more time to collapse onto a single adiabatic state. Clearly, the construction of this σ parameter is important for recovery of correct electronic dynamics. Surprisingly, this doesn't seem to have much of an effect on the resulting populations. However, this is due to the fact in the limit of large σ CTMQC becomes identical to Ehrenfest dynamics and Ehrenfest dynamics captures the evolution of the adiabatic populations very well for each model, with the exception of model 4. It should also be noted that for small values of σ , propagation using CTMQC can become unstable due to a noisy nuclear density giving rise to an unstable quantum momentum term. A value of 0.6 bohr seems to provide the best fit to exact data. However, this may

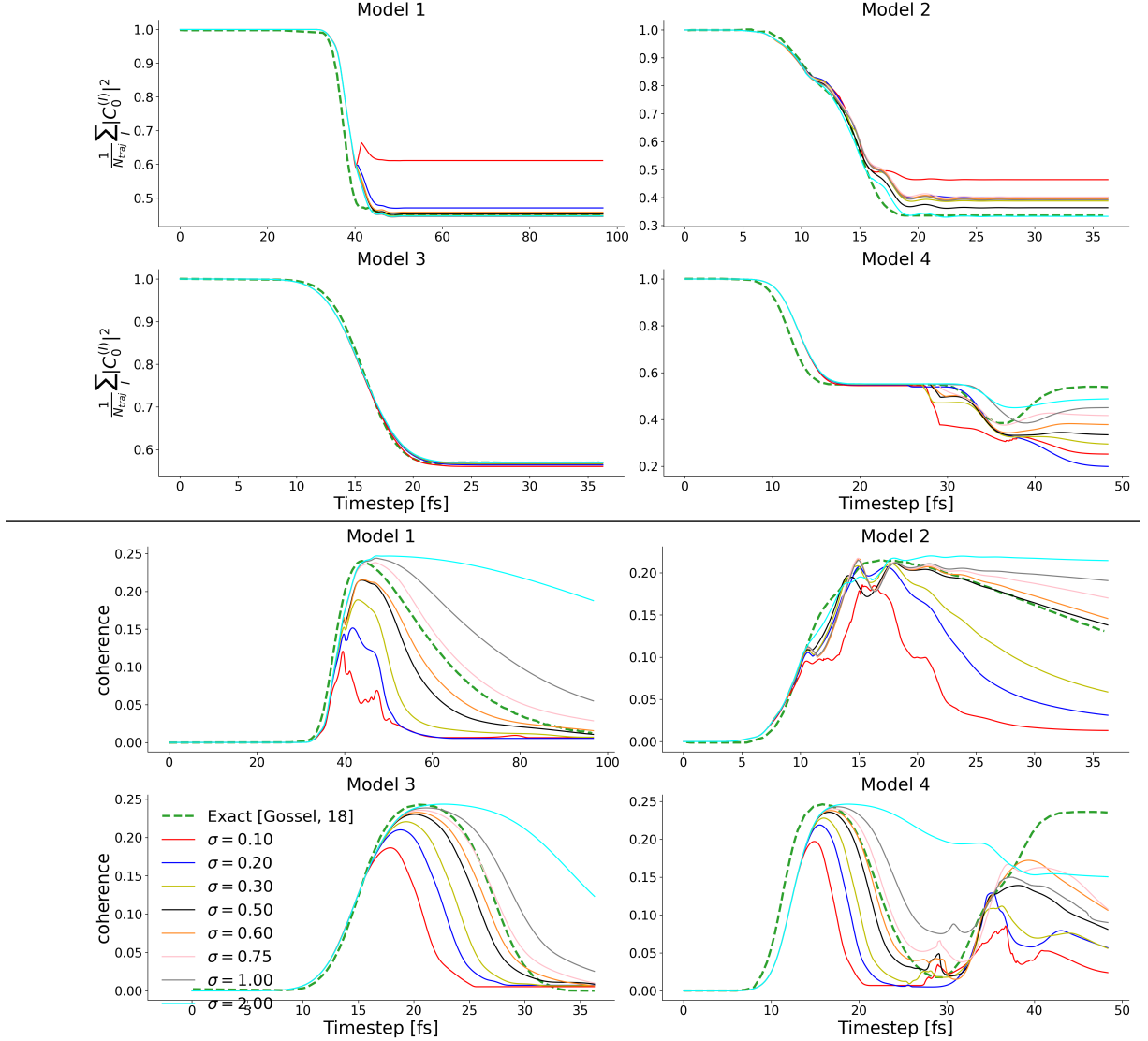


Figure 2.12: 4 high momenta cases of the Tully models with a various constant σ values used in the calculation of the quantum momentum. Thin solid lines show results from my simulations. The thick, green, dashed line shows data from exact simulations taken from Gossel, 18³.

not mean this is appropriate for all types of simulations.

2.3.2 Dynamic $\sigma_v^{(I)}(t)$ calculation

In the appendix of Gossel, 18³ an algorithm was outlined to calculate σ on-the-fly based on the density of replicas within a cutoff distance of each atom. This is given in appendix G. However, this method also relies on a constant parameter to calculate σ so doesn't remove a parameter, though the resulting dynamics do not seem as sensitive to changes in this parameter as in σ itself.

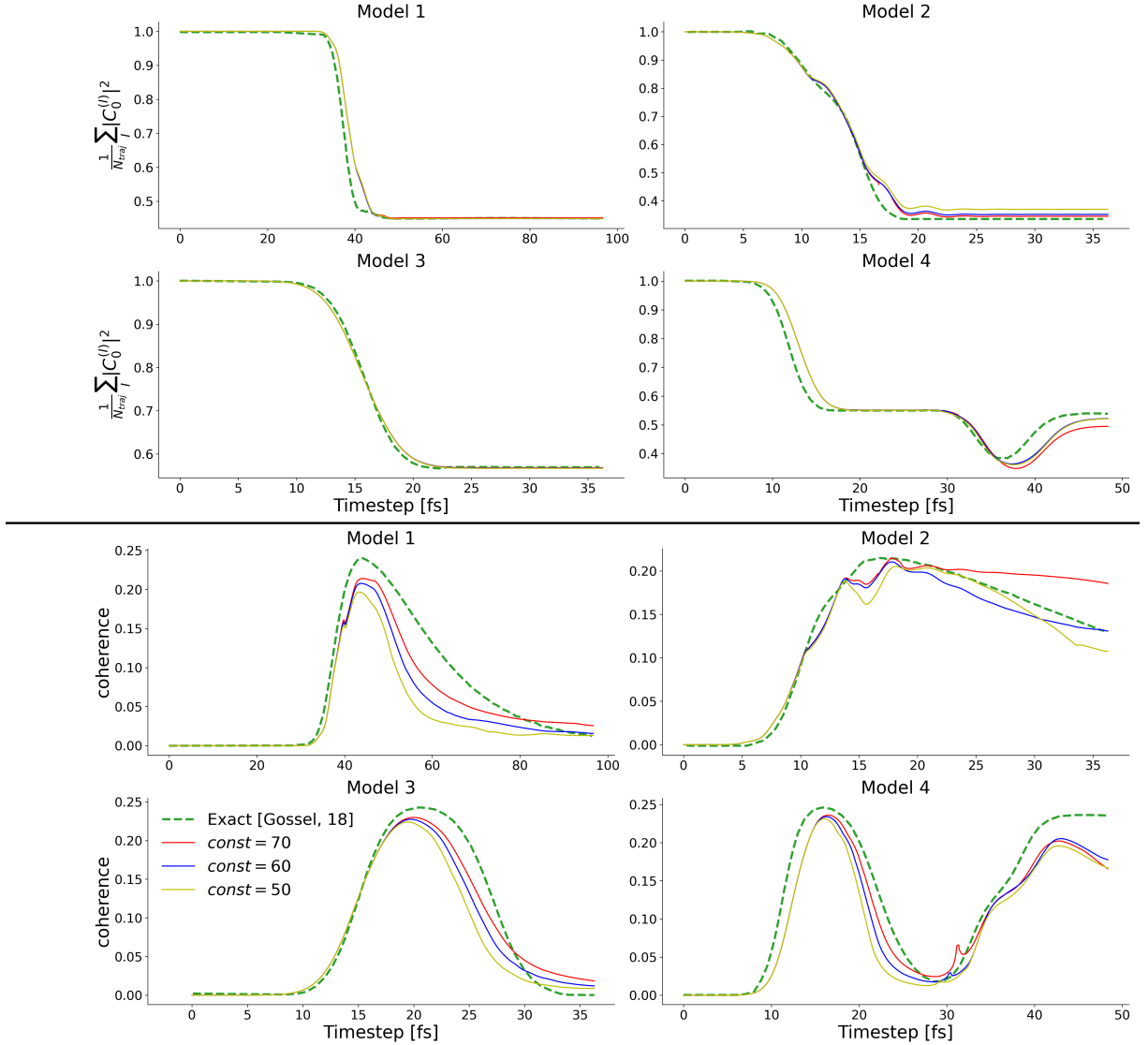


Figure 2.13

Figure 2.13 shows populations and coherences for the 4 (high momentum) Tully models with various values of const . It is encouraging to see populations now resemble exact results more closely. This is especially true in model 4, where the dip in the populations is recovered. All 3 constants give nearly identical populations, though a constant of 60 seems to give results that most closely resemble the exact coherences. However, seeing as this (like the width parameter) is not a physical parameter it is hard to know if this is reasonable for all systems.

2.4 Conclusion

In this chapter I have reported results from my implementation of the CTMQC equations applied to the Tully models. The Tully models are a set of 4 Hamiltonians dictating the motion of 1 atom in 1 dimension. These models are commonly simulated as they are simple enough to be solved analytically and complex enough to provide a reasonable test for any new nonadiabatic molecular dynamics (NAMD) technique. I have shown results from various tests which validate my implementation and shown how well CTMQC conserves the norm of the wavefunction and total energy, with the latter showing some concerning results. I have also highlighted 2 issues with the dynamics in CTMQC. These are the sudden divergences in the quantum momentum term and the ambiguity surrounding the calculation of the gaussian width parameter, σ . I have given a method designed to address the former issue, which has been shown to significantly improve the norm conservation. The latter problem has been touched upon in the literature, though no thorough studies have been reported.

The propagation of the CTMQC equations using a model Hamiltonian is a good first step in implementing a new NAMD technique. Its relative simplicity allows for a close inspection of each of the quantities involved in the propagation, especially new quantities such as the adiabatic momentum term, $\mathbf{f}_{l,v}^{(I)}$ and the quantum momentum term, $\mathcal{Q}_{lk,v}^{(I)}$. The same code used to simulate the Tully model system can also be used as a base for future extensions such as in 3D or many atom systems. However, before such extensions are implemented a new way to construct the Hamiltonian is needed. In the next chapter I will discuss my implementation of CTMQC within the fragment orbital based framework which relies on the fast calculation of the Hamiltonian using a finite difference method for off-diagonals and a classical force-field to calculate diagonal terms.

Chapter 3

CTMQC applied to molecular systems

In order to apply CTMQC to large molecular systems (hundreds of molecules) a new way to construct the Hamiltonian is needed. In this work I have implemented the CTMQC equations within the fragment-orbital based framework. This relies on the equations being expressed in a pseudo-diabatic basis and the Hamiltonian being constructed in 2 parts: the diagonal elements (site energies) and the off-diagonals (electronic couplings). The basis is termed 'pseudo-diabatic' due to the fact that non-adiabatic coupling vectors are small but non vanishing, this results in a basis where the excess charge carrier is strongly but not strictly localised on a single molecule. Within the Hamiltonian, the site energies are calculated via classical force-fields and the electronic couplings are calculated via the analytic overlap method^{58,60} (AOM). In this method the coupling elements are assumed to be proportional to the overlap between the highest singly occupied molecular orbitals (SOMO) on the donor and acceptor molecules (see equation (3.1)). This approximation is often used in the literature, e.g. in the fragment orbital density functional theory^{64–66} (FODFT) method and has been shown to be valid for π -conjugated molecules^{58,67}.

$$H_{ab} = C\langle \varphi_a | \varphi_b \rangle = CS_{ab} \quad (3.1)$$

Where $\varphi_{a(b)}$ represents a singly occupied molecular orbital on the donor (acceptor) and C is the scaling constant and comes from DFT parameterisation. The singly occupied molecular orbitals are calculated as a linear combination of Slater-type orbitals (STO) as in equation (3.2). In this equation we loop over each atom in the molecule and sum

the size of the contribution, $c_{p\pi,i}$, multiplied by the STO, $p_{\pi,j}$. In this case the STO is represented by a p-orbital. The size of the p-orbital on each atom, $c_{p\pi,i}$, is parameterised before the simulation with DFT.

$$|\varphi_{mol}\rangle = \sum_{i \in mol}^{N_{atoms}} c_{p\pi,i} |p_{\pi,i}\rangle \quad (3.2)$$

Importantly, the AOM method offers a very fast way to calculate the off-diagonal elements of the hamiltonian via a finite-difference method with an accuracy comparable to that of DFT methods. This has been implemented within an open-source software package named CP2K and is used by a fragment-orbital based surface hopping technique to study large systems of hundreds of molecules. In the next chapter the surface hopping technique will be discussed in further detail and applied to a system of pentacene molecules in order to investigate charge carrier (hole) transfer within amorphous systems.

3.1 Basis Transformation

In order to use the FOB method, as stated above the CTMQC equations in the adiabatic basis must be transformed to the diabatic basis. In the following derivation C_l will represent the adiabatic expansion coefficient corresponding to state l and u_l will represent the orthogonal diabatic expansion coefficients.

The CTMQC equations in the adiabatic basis are given below in equation (3.3) of the forces and (3.4) coefficients:

$$\begin{aligned} \mathbf{F}_v^{(I)} = & - \sum_k |C_k^{(I)}|^2 \nabla_v E_k^{(I)} - \sum_{k,l} C_l^{*(I)} C_k^{(I)} \left(E_k^{(I)} - E_l^{(I)} \right) \mathbf{d}_{v,lk}^{ad,(I)} \\ & - \sum_{l,k} |C_l^{(I)}|^2 \left(\sum_{v'}^{N_n} \frac{2}{\hbar M_{v'}} \mathcal{D}_{v',lk}^{(I)} \cdot \mathbf{f}_{l,v'}^{(I)} \right) [\mathbf{f}_{k,v}^{(I)} - \mathbf{f}_{l,v}^{(I)}] |C_k^{(I)}|^2 \end{aligned} \quad (3.3)$$

$$\begin{aligned}\dot{C}_l^{(I)} = & -\frac{i}{\hbar}E_l^{(I)}C_l^{(I)} - \sum_k C_k^{(I)} \sum_{v=1}^{N_n} \frac{\mathbf{P}_v^{(I)}}{M_v} \cdot \mathbf{d}_{v,lk}^{ad,(I)} \\ & - \sum_{v=1}^{N_n} \sum_k \frac{\mathcal{Q}_{v,lk}^{(I)}}{\hbar M_{v'}} \cdot [\mathbf{f}_{k,v}^{(I)} - \mathbf{f}_{l,v}^{(I)}] |C_k^{(I)}|^2 C_l^{(I)}\end{aligned}\quad (3.4)$$

Where:

- $E_k^{(I)}$ is the adiabatic energy for state k and trajectory I
- $C_k^{(I)}$ is the adiabatic expansion coefficient for state k and trajectory I
- $\mathbf{P}_v^{(I)}$ is the classical momentum of atom v on trajectory I
- $\mathbf{d}_{v,lk}^{ad,(I)}$ is the nonadiabatic coupling vector (given in the adiabatic basis)
- M_v is the mass of nuclei v
- $\mathcal{Q}_{v,lk}^{(I)}$ is the quantum momentum vector for atom v corresponding to the lk pair of states in trajectory I
- $\mathbf{f}_{l,v}^{(I)}$ is the adiabatic momentum on state l , atom v and trajectory I

3.1.1 Coefficients

To transform the equation for the propagation of the coefficients it is far neater to use the notation of linear algebra as in equation (3.5) below:

$$\dot{\mathbf{C}}^{(I)} = \mathbb{X}_v^{(I)} \mathbf{C}^{(I)} = \left(\mathbb{X}_{eh,v}^{(I)} + \mathbb{X}_{qm,v}^{(I)} \right) \mathbf{C}^{(I)} \quad (3.5)$$

Where the \mathbb{X} matrices are defined as in equations (3.6) and (3.7) below.

$$\mathbb{X}_{lk,v}^{eh(I)} = -\frac{i}{\hbar}E_l^{(I)} - \sum_v \frac{\mathbf{P}_v^{(I)}}{M_v} \cdot d_{lk,v}^{ad,(I)} \quad (3.6)$$

$$\mathbb{X}_{ll,v}^{qm(I)} = - \sum_{v=1}^{N_n} \sum_k \frac{\mathcal{Q}_{v,lk}^{(I)}}{\hbar M_{v'}} \cdot [\mathbf{f}_{k,v}^{(I)} - \mathbf{f}_{l,v}^{(I)}] |C_k^{(I)}|^2 \quad (3.7)$$

Using the identities:

$$\mathbb{U}^{-1} = \mathbb{U}^\dagger \quad (3.8)$$

$$\mathbf{C}^{(I)} = \mathbb{U}^{\dagger(I)} \mathbf{u}^{(I)} \quad (3.9)$$

$$\dot{\mathbf{C}}^{(I)} = \mathbb{U}^{\dot{\dagger}(I)} \mathbf{u}^{(I)} + \mathbb{U}^{\dagger(I)} \dot{\mathbf{u}}^{(I)} \quad (3.10)$$

Where $\mathbb{U}^{(I)} = \langle \phi_l^{(I)} | \psi_n^{(I)} \rangle$ is the unitary transformation matrix transforming from the diabatic to adiabatic basis. The $\mathbf{u}^{(I)}$ terms are the diabatic expansion coefficients on trajectory I.

After some algebra we arrive at:

$$\dot{\mathbf{u}}^{(I)} = \underbrace{\left(\mathbb{U}^{(I)} \mathbb{X}_{eh} \mathbb{U}^{\dagger(I)} + \mathbb{U}^{(I)} \mathbb{U}^{\dagger(I)} \right) \mathbf{u}^{(I)}}_{\text{Ehrenfest}} + \underbrace{\left(\mathbb{U}^{(I)} \mathbb{X}_{qm} \mathbb{U}^{\dagger(I)} \right) \mathbf{u}^{(I)}}_{\text{Quantum Momentum}} \quad (3.11)$$

In equation (3.11) I've separated the contribution from Ehrenfest and the contribution from the new quantum momentum terms. The Ehrenfest part can be shown to reduce to a simpler form (see Spencer, 2016⁶⁰ and Carof, 17⁶⁸ for more details). The quantum momentum term must be coded up as shown -with the transformation matrices. This gives the final equation for the propagation of the diabatic expansion coefficients, shown in equation (3.12).

$$\dot{\mathbf{u}}^{(I)} = \left(-\frac{i}{\hbar} \mathbb{H}^{(I)} - \mathbb{D}_{diab}^{(I)} \right) \mathbf{u}^{(I)} + \left(\mathbb{U}^{(I)} \mathbb{X}_{qm} \mathbb{U}^{(I)} \right)^{-1} \mathbf{u}^{(I)} \quad (3.12)$$

Where $\mathbb{H}^{(I)}$ is the diabatic Hamiltonian constructed via the AOM method, $\mathbb{D}_{diab}^{(I)}$ are the diabatic nonadiabatic coupling elements ($d_{diab,lk}^{(I)} = \langle \phi_l | \dot{\phi}_k \rangle$).

3.1.2 Forces

A full derivation of the transformation of basis for the equation propagating forces is given in appendix H. The result is given in equation (3.13) below:

$$\begin{aligned} \mathbf{F}_{eh,v}^{(I)} = & \sum_{i,j} \mathbf{u}_i^{*(I)} \mathbf{u}_j^{(I)} \left(\nabla_v H_{ij}^{(I)} + \sum_l \mathbf{d}_{lk,v}^{(I)} H_{lj}^{(I)} - \sum_l \mathbf{d}_{lj,v}^{(I)} H_{il} \right) \\ & - \sum_{l,k} |C_l^{(I)}|^2 \left(\sum_{v'}^{N_n} \frac{2}{\hbar M_{v'}} \mathcal{Q}_{v',lk}^{(I)} \cdot \mathbf{f}_{l,v'}^{(I)} \right) [\mathbf{f}_{k,v}^{(I)} - \mathbf{f}_{l,v}^{(I)}] |C_k^{(I)}|^2 \end{aligned} \quad (3.13)$$

There are a couple of things to note with this equation. Firstly, (as in the coefficients equation) the quantum momentum part has not been transformed. This is because the forces are basis independent and don't need to be transformed. Secondly, the quantities required for the calculation of this part of the equation are already calculated in order to propagate the coefficients so only a small amount of extra effort is required to calculate the quantum momentum force term. The Ehrenfest part of the equation has been transformed. This is because the nonadiabatic coupling vectors within the adiabatic basis are never required so are never calculated. The Ehrenfest force term requires these nonadiabatic coupling vectors so would add extra computational overheads. Further, the commutator term in the diabatic basis has been shown to provide a negligible contribution to the overall force. This term requires significant computational effort and can be neglected. This makes the calculation of the Ehrenfest forces in the diabatic basis far cheaper than in the adiabatic basis.

3.2 Testing the diabatic propagator

The diabatic propagation can be tested against the already tested adiabatic propagator using the Tully model Hamiltonian. The code should give the same results, given the same inputs. To check this, in figure 3.1, the simulations carried out in figure 2.11 were repeated though this time the diabatic propagator was used. We can see in figure 3.1 that the results for the adiabatic and diabatic propagator are almost exactly the same for each model. In model 3, where the problem with the divergent $\mathcal{Q}_{lk,v}^{(I)}$ doesn't occur, the 2 results are exactly on top of each other. In the other models there is a slight discrepancy. This is due to the unpredictable $\mathcal{Q}_{lk,v}^{(I)}$ spikes not being perfectly corrected. However,

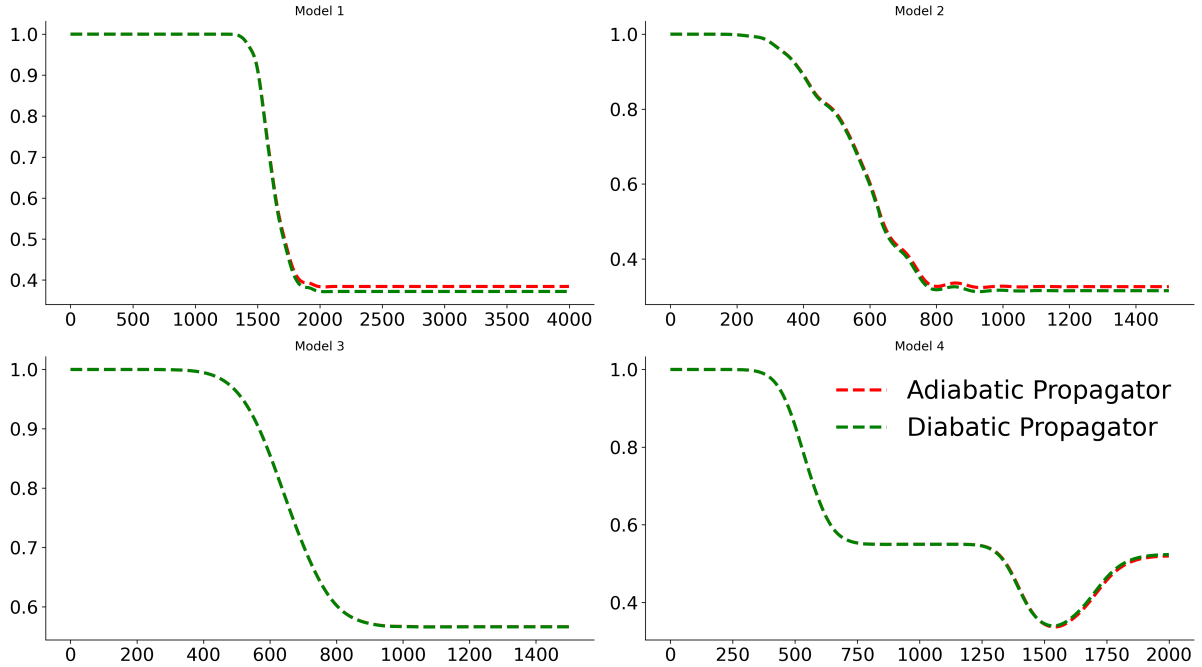


Figure 3.1: The 4 Tully models simulated using propagating the equations within a diabatic and adiabatic basis. The green line shows results from the diabatic propagator and the red line shows results from the adiabatic propagator.

figure 3.1 still serves as confirmation of the propagation within the diabatic basis.

3.3 Simulating Molecular Systems

To go beyond the 1D Tully model systems the AOM method is combined with CTMQC and applied to an Ethylene dimer. Fortunately, the majority of the code from the Tully model systems can be re-used. In fact, the only difference is the way the Hamiltonian (and diabatic NACE) is constructed. The code for carrying out these tasks (the AOM part) has been implemented by previous members of the group and has been well tested and verified against the literature and experimental studies. Therefore, I will not include any tests of this part of the code in this document but instead refer the reader to the numerous papers discussing AOM and its use in within the fewest switches surface hopping framework^{14,69–78}. An ethylene dimer was chosen as a reasonable first system due to its relative simplicity (shown in figure 3.2) the total number of atoms is 12 and only 2 electronic states will be considered. The system shown in figure 3.2 was initialised in the adiabatic ground state. Positions and velocities were sampled from a short NVT

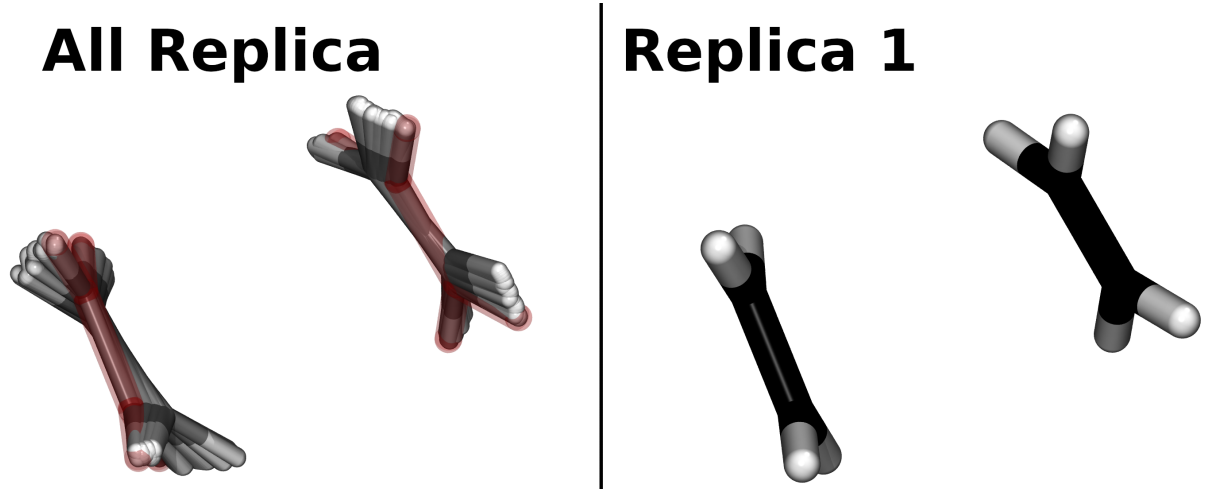


Figure 3.2: An example Ethylene dimer used to test the CTMQC implementation. The right panel shows the positions of just 1 replica. The left panel shows the positions of all replica with the replica shown on the right highlighted in red.

molecular dynamics equilibration. The scaling factor (C in equation (3.1)) was chosen to give a coupling of approximately 27 meV. This is approximately $\frac{1}{4} \times$ the reorganisation energy -parameterised to be 100 meV. The amount of charge transfer is dependent on the ratio between reorganisation energy and the electronic couplings ($\frac{H_{ab}}{\lambda}$). The factor of $\frac{1}{4}$ was chosen to be a reasonable factor -seen in other organic semiconducting systems. The nuclear timestep was chosen to be 0.05fs and the electronic one was 0.005 fs. The switch to $\mathbf{R}_{0,v}^{(I)}$ was chosen as the correction method of the quantum momentum and 100 trajectories were used. A constant σ of 0.7 was used as the dynamic σ tended to either vanish to 0 or blow up to a very large number.

In figure 3.3 the norm of the diabatic expansion coefficients are plotted, from the system described above. In this figure we see large jumps in the norm, these are caused by the divergences in the quantum momentum term. These occur more in this system than in the Tully models as it is more complex (more atoms, higher dimensional) and runs for a longer time with more avoided crossings. The fact that there are 12 atoms and 3 Cartesian dimensions instead of 1 means that the $\mathbf{R}_{lk,v}^{(I)}$ term must be calculated many more times increasing the probability of happening upon a divergence. The errors can also accumulate meaning that after a few trivial crossings the populations become extremely noisy. This eventually causes the code to crash and results from it cannot be

trusted. Most commonly the reason for the code crashing is a large spike in the computed forces caused by a spike in the quantum momentum. This large force then causes the atoms to collide and the code to crash. The code is very stable when just using Ehrenfest dynamics. Many more simulations have been carried out to diagnose and fix this issue.

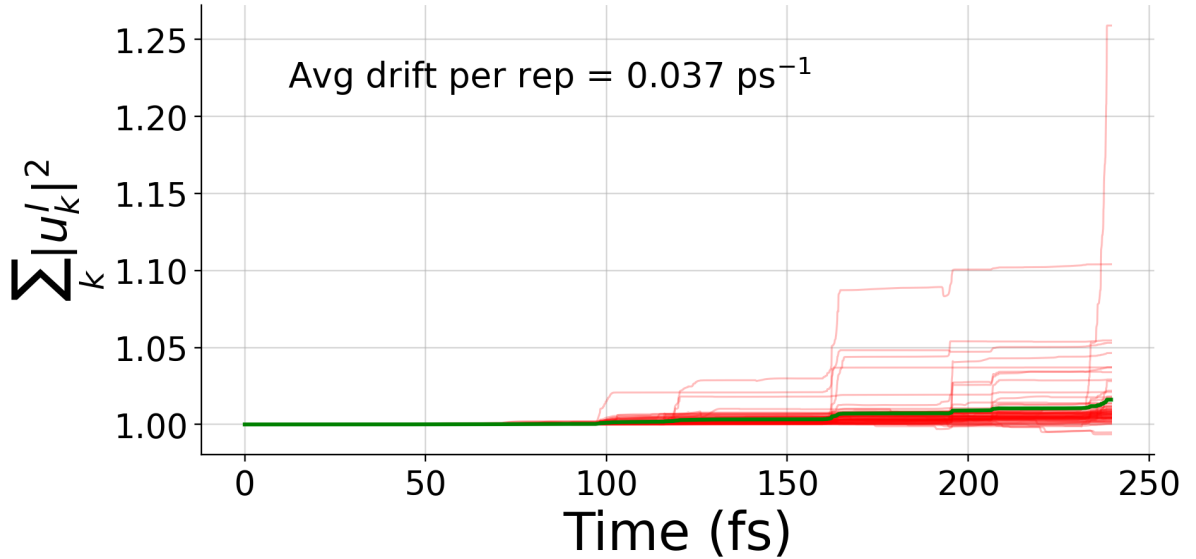


Figure 3.3: The norm of the adiabatic expansion coefficients. Thin red lines show the norm for each trajectory and the thick green line shows the average over all trajectories.

Results from all of these cannot be included in this document though I will provide a brief summary of results below.

3.3.1 Varying the number of replicas

Increasing the number of replicas in the system, somewhat counterintuitively, decreases stability. This is because with more replicas there is more of a chance the code will stumble upon a calculation giving a divergence in the quantum momentum term.

3.3.2 Varying the timestep

Decreasing the timestep does help to improve norm conservation (before the code crashes). However, it does not lead to a more stable simulation that allows for longer timescales to be simulated. This is because decreasing the timestep provides more opportunity for

a small numerical error to cause a divergence in the quantum momentum term.

3.3.3 Removing Center of Mass Motion

In some simulations the replicas positions spread out so much that the quantum momentum term became negligible. This was to prevent that from happening.

3.3.4 Varying the gaussian width (σ) parameter

If the σ parameter is set to be large (> 2) then the simulation is more stable as the quantum momentum term is smaller and errors don't accumulate as quickly. However, this the limit of a very large σ is Ehrenfest dynamics. If the σ is set to be small (< 0.2) the simulation becomes extremely unstable as the quantum momentum forces populations to decohere too quickly. This is discussed in more detail in section 2.3.

3.3.5 Turning off the quantum momentum addition to the force term

The code runs more stably if the quantum momentum term is not included in the forces. This has also been shown to be much less important for the accuracy of the results than the quantum momentum addition to the coefficients. However, even in this case the code eventually crashes after an accumulation of errors in the coefficients results in erroneous forces resulting in geometries that fail CP2K internal checks.

3.3.6 Renormalisation

This does not seem to help with stability. Furthermore, it merely helps hide the large norm drift and doesn't fix the problems it causes.

3.4 Conclusions

The CTMQC method shows great promise as a new nonadiabatic molecular dynamics (NAMD) technique. It was derived as the semi-classical limit of the exact factorisation of the time-dependent electron-nuclear wave function^{47,48}. It purports to handle decoherence corrections in a more rigorous, first principles way without the need of empirical

parameters. Although this method was first reported in 2015⁴⁸, there are still very few papers reporting results using this method^{3,48,56}. With the most complex system being restricted to a 7 atom molecule⁵⁶. I believe this is due to the problems with the current formalism. Before, the widespread acceptance of CTMQC as a standard nonadiabatic molecular dynamics method 2 critical flaws must be addressed. First is the calculation of the gaussian width parameter, σ and the second is the divergence of the quantum momentum term. It would be possible to further investigate the width parameter, perhaps through benchmarks against higher level calculations to establish a relationship between characteristics of the system and the width parameter. From a short investigation using the Tully models it seems a constant width parameter gives reasonable results and it should be set to be between 0.2 and 0.5. This problem does not seem intractable. However, it may be harder to correct for the large divergences in the quantum momentum caused by the denominator of the quantum momentum intercept term, $\mathbf{R}_{lk,v}$ approaching zero. This causes the code to become unstable for even simple molecular systems. In the 1D Tully models this could be corrected by switching to an alternative intercept, $\mathbf{R}_{0,v}^{(I)}$. However, this alternative intercept results in unphysical population transfer in regions of zero nonadiabatic coupling so cannot be used throughout the simulation.

Both these problems can both be traced back to the construction of the nuclear density from the nuclear positions. The method explored in this thesis is the method reported in the literature. That involved placing a gaussian function centered on each atomic position with a certain width, σ to smear out the position and give a smooth nuclear distribution. I believe that exploring alternative technique to construct the nuclear density from atomic positions may lead to the largest improvements in the CTMQC technique. Perhaps even allowing one to study complex molecular systems with many nonadiabatic coupling regions such as those typically found in charge transfer studies.

In this chapter I have implemented and tested a working version of CTMQC in both CP2K and as a standalone python script. These are both available for downloading from the author's github page at: <https://github.com/95ellismle>. I have given the CTMQC

equations in an orthogonal diabatic basis and linked it to the AOM method, which provides a fast way of calculating electronic couplings within the Hamiltonian. I have also highlighted what I believe to be the largest problems facing CTMQC. However, as these problems may require an entire PhD project in themselves, I have not addressed them in much detail. In the rest of this work I will discuss an alternative NAMD technique, namely fewest switches surface hopping, and apply it to large molecular system to get experimentally verifiable results.

Appendix A

Tully Model Paramters

A.1 Model 1 -Single Avoided Crossing

	Quantity	Value	Unit
Hamiltonian Paramters:			
$H_{11}(\mathbf{R}) = A \tanh(B\mathbf{R})$	Initial Position	-20	a.u.
$H_{12}(\mathbf{R}) = Ce^{-D\mathbf{R}^2}$	Initial Velocities	15.0, 25.0	a.u.
$H_{21}(\mathbf{R}) = H_{12}(\mathbf{R})$	Initial Adiab Pop	ground state	-
$H_{22}(\mathbf{R}) = -H_{11}(\mathbf{R})$	Simulation Time	6000, 4000	a.u.
Where A = 0.03, B = 0.4, C = 0.005 and D = 0.3	$\sigma_v^{(I)}$	0.5	a.u.
	M (σ constant)	40	-
	$\Delta t_{\text{nuclear}}$	0.1	fs
	$\Delta t_{\text{electronic}}$	0.01	fs
	$\frac{\delta \mathbf{R}_{lk,v}^{(I)}}{\delta t}$ threshold	0.15	a.u.
	N_{rep}	200	-

A.2 Model 2 -Dual Avoided Crossing

	Quantity	Value	Unit
Hamiltonian Paramters:			
$H_{11}(\mathbf{R}) = 0$	Initial Position	-8	a.u.
$H_{12}(\mathbf{R}) = Ce^{-D\mathbf{R}^2}$	Initial Velocities	16.0, 30.0	a.u.
$H_{21}(\mathbf{R}) = H_{12}(\mathbf{R})$	Initial Adiab Pop	ground state	-
$H_{22}(\mathbf{R}) = -Ae^{-B\mathbf{R}^2} + E$	Simulation Time	2500, 1500	a.u.
Where A = 0.1, B = 0.28, C = 0.015, D = 0.06 and E = 0.05	$\sigma_v^{(I)}$	0.5	a.u.
	M (σ constant)	40	-
	$\Delta t_{\text{nuclear}}$	0.1	fs
	$\Delta t_{\text{electronic}}$	0.01	fs
	$\frac{\delta \mathbf{R}_{ik,v}^{(I)}}{\delta t}$ threshold	0.15	a.u.
	N_{rep}	200	-

A.3 Model 3 -Extended Coupling

	Quantity	Value	Unit
Hamiltonian Paramters:			
$H_{11}(\mathbf{R}) = A$	Initial Position	-15	a.u.
$H_{12}(\mathbf{R}) = \begin{cases} Be^{C\mathbf{R}}, & R \leq 0 \\ B(2 - e^{-C\mathbf{R}}), & R > 0 \end{cases}$	Initial Velocities	10, 30	a.u.
$H_{21}(\mathbf{R}) = H_{12}(\mathbf{R})$	Initial Adiab Pop	ground state	-
$H_{22}(\mathbf{R}) = -H_{11}(\mathbf{R})$	Simulation Time	5000, 1500	a.u.
Where A = 6×10^{-4} , B = 0.1 and C = 0.9	$\sigma_v^{(I)}$	0.5	a.u.
	M (σ constant)	40	-
	$\Delta t_{\text{nuclear}}$	0.1	fs
	$\Delta t_{\text{electronic}}$	0.01	fs
	$\frac{\delta \mathbf{R}_{ik,v}^{(I)}}{\delta t}$ threshold	0.15	a.u.
	N_{rep}	200	-

A.4 Model 4 -Dual Arch

Hamiltonian Paramters:

$$H_{11}(\mathbf{R}) = A$$

$$H_{12}(\mathbf{R}) = \begin{cases} B \left[-e^{C(\mathbf{R}-D)} + e^{C(\mathbf{R}+D)} \right] & R \leq -D \\ B \left[e^{-C(\mathbf{R}-D)} - e^{-C(\mathbf{R}+D)} \right] & R \geq D \\ B \left[2 - e^{C(\mathbf{R}-D)} - e^{-C(\mathbf{R}+D)} \right] & -D < R < D \end{cases}$$

$$H_{21}(\mathbf{R}) = H_{12}(\mathbf{R})$$

$$H_{22}(\mathbf{R}) = -H_{11}(\mathbf{R})$$

Where $A = 6 \times 10^{-4}$, $B = 0.1$, $C = 0.9$ and

$$D = 4$$

Quantity	Value	Unit
Initial Position	-20	a.u.
Initial Velocities	10, 40	a.u.
Initial Adiab Pop	ground state	-
Simulation Time	6000, 2000	a.u.
$\sigma_v^{(I)}$	0.5	a.u.
M (σ constant)	40	-
$\Delta t_{\text{nuclear}}$	0.1	fs
$\Delta t_{\text{electonic}}$	0.01	fs
$\frac{\delta \mathbf{R}_{lk,v}^{(I)}}{\delta t}$ threshold	0.15	a.u.
N_{rep}	200	-

Appendix B

Wigner Distribution Derivation

The nuclear wavepacket (at time 0) is given by:

$$\chi(R) = \frac{1}{(\pi\mu^2)^{\frac{1}{4}}} e^{-\frac{(R-R_0)^2}{2\mu^2} + ik_0(R-R_0)} \quad (\text{B.1})$$

The Wigner quasiprobability function for momentum and position (p, R) is given by:

$$W(p, R) = \frac{1}{\pi\hbar} \int_{-\infty}^{\infty} \chi^*(R+y)\chi(R-y)e^{\frac{2ipy}{\hbar}} dy \quad (\text{B.2})$$

However, both Ehrenfest and CTMQC require atomic positions as input so we must extract the position and velocity probability densities from this. We get these from the marginal integrals of the Wigner distribution i.e.

$$|f(R)|^2 = \int_{-\infty}^{\infty} W(R, p) dp \quad (\text{B.3})$$

$$|f(p)|^2 = \int_{-\infty}^{\infty} W(R, p) dR \quad (\text{B.4})$$

In order to calculate these marginal integrals we must first crunch through the maths of equation (B.2). Substituting eq (B.1) into (B.2):

$$W(p, R) = \frac{1}{\pi\hbar} \int_{-\infty}^{\infty} \frac{1}{\mu\sqrt{\pi}} e^{-\frac{(R+y-R_0)^2}{2\mu^2} - 2ik_0y - \frac{(R-y-R_0)^2}{2\mu^2}} e^{\frac{2ipy}{\hbar}} dy \quad (\text{B.5})$$

Simplifying the 2 quadratic equations (equation (B.5)) we get:

$$W(p, R) = \frac{1}{\pi \hbar} \int_{-\infty}^{\infty} \frac{1}{\mu \sqrt{\pi}} e^{-\mu^{-2}(y^2 - 2ik_0 y \mu^2 + (R-R_0)^2)} e^{\frac{2ipy}{\hbar}} dy \quad (\text{B.6})$$

We can now take the expressions not dependant on y outside of the integral and combine the exponents.

$$W(p, R) = \frac{1}{\pi \sqrt{\pi} \mu \hbar} e^{-\frac{(R-R_0)^2}{\mu^2}} \int_{-\infty}^{\infty} e^{-\frac{y^2 + 2iy\mu^2(\frac{p}{\hbar} - k_0)}{\mu^2}} dy \quad (\text{B.7})$$

Integrating we get:

$$\int e^{-\frac{y^2 + 2iy\mu^2(\frac{p}{\hbar} - k_0)}{\mu^2}} dy = \frac{\sqrt{\pi} \mu}{2} e^{-\frac{\mu^2}{\hbar^2}(p - \hbar k_0)^2} \operatorname{erf} \left[\frac{y}{\mu} + i \left(\frac{p\mu}{\hbar} - \mu k_0 \right) \right] \quad (\text{B.8})$$

Applying limits we get:

$$\int_{-\infty}^{\infty} e^{-\frac{y^2 + 2iy\mu^2(\frac{p}{\hbar} - k_0)}{\mu^2}} dy = \sqrt{\pi} \mu e^{-\frac{\mu^2}{\hbar^2}(p - \hbar k_0)^2} \quad (\text{B.9})$$

Substituting this back into the Wigner distribution (equation (B.2)) we finally get:

$$W(p, R) = \frac{1}{\pi \hbar} e^{-\frac{(R-R_0)^2}{\mu^2}} e^{-\frac{(p - \hbar k_0)^2}{\hbar^2/\mu^2}} \quad (\text{B.10})$$

Taking the marginal integrals we get the position and velocity probability distributions:

$$|f(R)|^2 = \frac{2}{\mu \sqrt{\pi}} e^{-\frac{(R-R_0)^2}{\mu^2}} \quad (\text{B.11})$$

$$|f(p)|^2 = \frac{2}{\frac{\hbar}{\mu} \sqrt{\pi}} e^{-\frac{\mu^2}{\hbar^2}(p - \hbar k_0)^2} \quad (\text{B.12})$$

The above distributions are randomly sampled to get initial atomic velocities and positions for each simulation.

Appendix C

$\mathbf{R}_{lk,v}$ Alternatives

C.1 $\mathbf{R}_{lk,v}$ Extrapolation

C.2 Alternative Quantum Momentum Intercept

In Agostini, 16² another quantum momentum intercept term is discussed. This term is not used because, as previously discussed in section 1.4, it leads to unphysical transfer of population between adiabatic states when the nonadiabatic coupling elements are 0. However, it can be used in these Tully Models as an effective fix to the discontinuities caused by the $\mathbf{R}_{lk,v}$ term.

The other quantum momentum intercept, $\mathbf{R}_{0,v}^{(I)}$, comes directly from the construction of the nuclear density using a linear combination of a product of gaussians (see equation (1.12) in the introduction). It is defined as in equation (C.1) below:

$$\mathbf{R}_{0,v}^{(I)} = \sum_{J}^{N_{tr}} \left[\frac{\hbar \prod_{v'} g_{\sigma_{v'}^{(J)}(t)} \left(\mathbf{R}_{v'}^{(I)}(t) - \mathbf{R}_{v'}^{(J)}(t) \right)}{2 \sigma_v^{(J)}(t)^2 \sum_{K}^{N_{tr}} \prod_{v'} g_{\sigma_{v'}^{(K)}(t)} \left(\mathbf{R}_{v'}^{(I)}(t) - \mathbf{R}_{v'}^{(K)}(t) \right)} \mathbf{R}_v^{(I)} \right] \quad (\text{C.1})$$

However, as switching to this intercept directly may cause discontinuities in itself a smoothing parameter is applied to ease the switch. This is given in equation (C.2) below:

$$[1 - A(t)] R_{good}(t) + A(t) R_{bad}(t) = R_{effective}(t) \quad (\text{C.2})$$

R_{good} refers to the intercept that should be switched to (e.g. for the detection of a spike in the $R_{lk,v}^{(I)}$ we switch to the intercept in in equation (C.1)). $R_{lk,v}^{(I)}$ refers to the intercept that is being switched from (e.g. when it is detected that the divergence of $R_{lk,v}^{(I)}$ has finished then we switch from the alternative intercept back to $R_{lk,v}^{(I)}$). $A(t)$ is a smoothing parameter and is given in equation (C.3) below:

$$A(t) = \frac{D_v^{(I)}}{2} \left[\tanh\left(t - \frac{t_{final} + t_{init}}{0.6Ndt}\right) + 1 \right] \quad (\text{C.3})$$

Where $D_v^{(I)}$ is the distance between the 2 intercepts (e.g. $D_v^{(I)} = R_{lk,v}^{(I)} - R_{0,v}^{(I)}$), N is the number of steps to take before settling solely on one intercept, t_{init} is the time of detection of the divergence, t_{final} is the time at which the code settles on 1 intercept and dt is the timestep taken.

A cartoon of this process is given in figure C.1

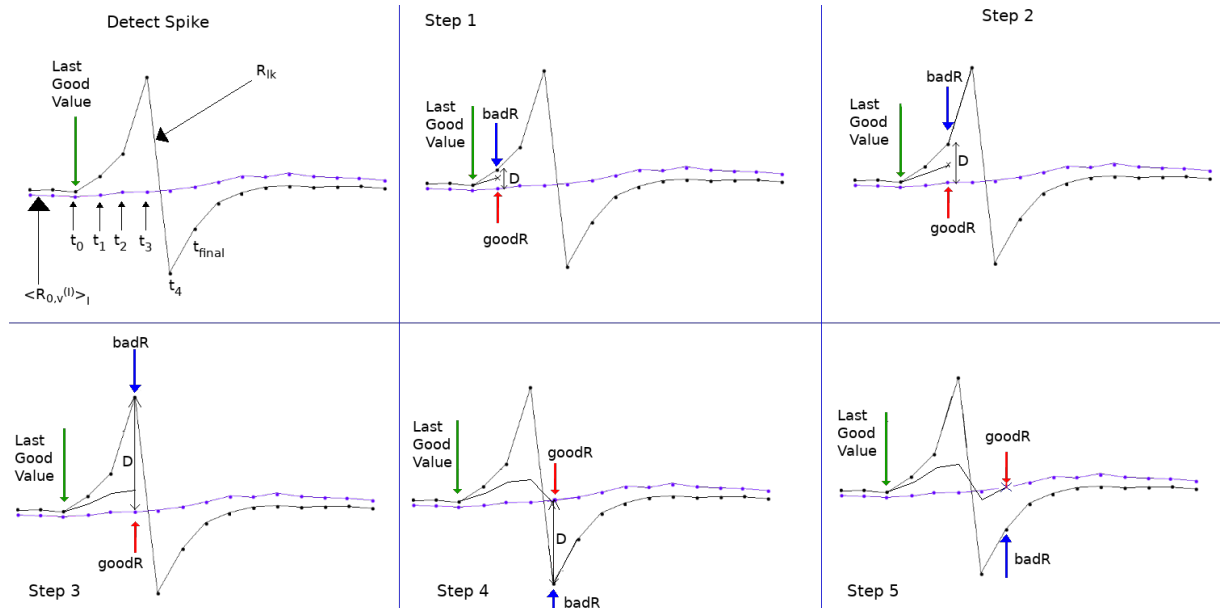


Figure C.1: A crude demonstration of the principle behind the smoothing procedure in switching between intercepts. The black line shows an intercept begin to diverge and the alternative intercept is shown in purple. As the step is incremented the amount of the alternative intercept that makes up the effective intercept is increased until only 1 intercept is used.

Appendix D

Rabi Oscillation

The time dependant Schrödinger equation is given below:

$$\hbar \frac{\delta}{\delta t} \Phi(\mathbf{R}(t), t) = \hat{H}(\mathbf{R}(t), t) \Phi(\mathbf{R}(t), t) \quad (\text{D.1})$$

If we hold the nuclear coordinates in place (e.g. remove time-dependence from nuclear coordinates) we get an ordinary differential equation as shown below:

$$\hbar \frac{d}{dt} \Phi(\mathbf{R}, t) = \hat{H}(\mathbf{R}, t) \Phi(\mathbf{R}, t) \quad (\text{D.2})$$

This has the following general solution. This can be solved with a Taylor series expansion.

$$\Phi(\mathbf{R}, t) = e^{\hbar \hat{H} t} \Phi(\mathbf{R}, 0)$$

Figure

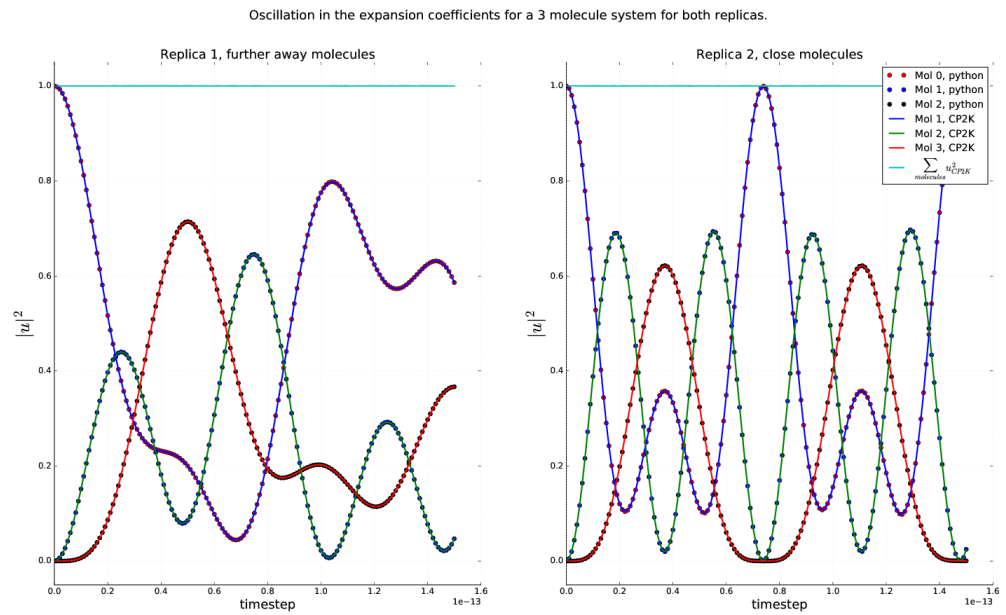


Figure D.1: Rabi oscillation occurring within a Ethylene trimer system. Dotted lines were calculated using equation (D.2), solid lines were calculated using the RK4 propagator within the CTMQC section of the CP2K code. The norm is shown on the top as a cyan line and the x axis shows the timestep in seconds.

Appendix E

Norm Conservation in CTMQC and Ehrenfest

A statement of the conservation of the norm, for a single trajectory, is given below in equation (E.1)

$$\frac{d}{dt} \sum_l |C_l(t)|^2 = \sum_l C_l^*(t) \frac{dC_l(t)}{dt} + \frac{dC_l^*(t)}{dt} C_l(t) = 2\mathbb{R} \left[\sum_l C_l(t)^* \frac{dC_l(t)}{dt} \right] \quad (\text{E.1})$$

Substituting the equation for the evolution of the adiabatic coefficients (and removing the purely imaginary term) into (??) we get equation (E.3)

$$\frac{d}{dt} \sum_l |C_l(t)|^2 = 2 \sum_l \mathbb{R} \left[\frac{-i}{\hbar} \cancel{\epsilon_{B\theta}^l} C_l(t)^* \cancel{C_l(t)} - \sum_k \left[C_l(t)^* C_k(t) d_{lk}^{ad} - (A_l - B_l) C_l(t)^* C_l(t) \right] \right] \quad (\text{E.2})$$

$$= -2 \sum_l \mathbb{R} \left[\sum_k \left[C_l(t)^* C_k(t) d_{lk}^{ad} - (A_l - B_l) C_l(t)^* C_l(t) \right] \right] \quad (\text{E.3})$$

Where:

$$A_l = \sum_{v=1}^{N_n} \sum_k \frac{\mathcal{Q}_{lk,v}(t)}{\hbar M_v} \cdot \mathbf{f}_{k,v}(t) |C_k(t)|^2 \quad (\text{E.4})$$

$$B_l = \sum_{v=1}^{N_n} \sum_k \frac{\mathcal{Q}_{lk,v}(t)}{\hbar M_v} \cdot \mathbf{f}_{l,v}(t) |C_k(t)|^2 \quad (\text{E.5})$$

The NACE term evaluates to 0 due to the anti-symmetry of the NACE giving us equation (E.7).

So far, we have proved that the norm should be conserved here for all terms apart from the quantum momentum terms i.e. Ehrenfest.

$$\frac{d}{dt} \sum_l |C_l^{QM}(t)|^2 = 2 \sum_l \Re[(A_l - B_l) C_l(t)^* C_l(t)] \quad (\text{E.6})$$

$$= 2 \left[\sum_l A_l |C_l(t)|^2 - \sum_l B_l |C_l(t)|^2 \right] \quad (\text{E.7})$$

However, $\sum_l A_l |C_l|^2 \equiv \sum_l B_l |C_l|^2$, therefore there is no change in the population and the norm should be conserved.

Appendix F

Energy Conservation in CTMQC

Definition:

$$\mathbf{A}_v = \sum_l |C_l|^2 \mathbf{f}_{l,v} + \hbar \mathbb{I} \left[\sum_{l,k} C_l^* C_k \mathbf{d}_{v,lk} \right]$$

$$\begin{aligned} \sum_v \frac{\mathbf{P}_v}{M_v} \cdot \mathbf{A}_v &= \sum_{l,v} |C_l|^2 \mathbf{v}_v \cdot \mathbf{f}_{l,v} + \hbar \mathbb{I} \left[\sum_{l,k,v} C_l^* C_k \mathbf{v}_{nu} \cdot \mathbf{d}_{lk,v} \right] \\ &= \sum_{l,v} \mathbf{v}_v |C_l|^2 \mathbf{f}_{l,v} + \hbar \mathbb{I} \left[\sum_{l,k} C_l^* C_k d_{lk} \right] \end{aligned}$$

$$\begin{aligned}
\langle \Phi | \dot{\Phi} \rangle &= \left\langle \sum_l C_l \psi_l \left| \frac{d}{dt} \left[\sum_k C_k \psi_k \right] \right. \right\rangle \\
&= \sum_l C_l^* \langle \psi_l | \sum_k \dot{C}_k \psi_k + \sum_k C_k \dot{\psi}_k \rangle \\
&= \sum_{l,k} C_l^* \dot{C}_k \langle \psi_l | \psi_k \rangle + \sum_{l,k} C_l^* C_k d_{lk} \\
&= \sum_l C_l^* \dot{C}_l + \sum_{l,k} C_l^* C_k d_{lk} \\
&= \mathbb{R} \left[\sum_l C_l^* \dot{C}_l \right] + \mathbb{I} \left[\sum_l C_l^* \dot{C}_l \right] + \sum_{l,k} C_l^* C_k d_{lk} \\
&= \frac{1}{2} \frac{d}{dt} \sum_l |C_l|^2 + \mathbb{I} \left[\sum_l C_l^* \dot{C}_l \right] + \sum_{l,k} C_l^* C_k d_{lk} \\
&= \mathbb{I} \left[\sum_l C_l^* \dot{C}_l \right] + \sum_{l,k} C_l^* C_k d_{lk}
\end{aligned}$$

$$\begin{aligned}
\langle \Phi | \hat{H} | \Phi \rangle &= \left\langle \sum_l C_l \psi_l | \hat{H} | \sum_k C_k \psi_k \right\rangle \\
&= \sum_{l,k} E_k C_l^* C_k \delta_{lk} \\
&= \sum_l E_l |C_l|^2
\end{aligned}$$

$$\begin{aligned}
E_{pot} &= \langle \Phi | \hat{H} | \Phi \rangle - \hbar \langle \Phi | \dot{\Phi} \rangle - \sum_v^{N_n} \frac{\mathbf{P}_v}{M_v} \mathbf{A}_v \\
&= \sum_l E_l |C_l|^2 - \hbar \mathbb{I} \left[\sum_l C_l^* \dot{C}_l \right] - \hbar \sum_{l,k} C_l^* C_k d_{lk} - \sum_{l,v} \mathbf{v}_v |C_l|^2 \mathbf{f}_{l,v} - \hbar \mathbb{I} \left[\sum_{l,k} C_l^* C_k d_{lk} \right] \\
&= \sum_l E_l |C_l|^2 - \hbar \mathbb{I} \left[\sum_l C_l^* \dot{C}_l \right] - \hbar \mathbb{I} \left[\sum_{l,k,v} C_l^* C_k \mathbf{v}_v \cdot \mathbf{d}_{lk} \right] - \sum_{l,v} \mathbf{v}_v |C_l|^2 \mathbf{f}_{l,v} = \sum_l E_l |C_l|^2 - \sum_{l,v} \mathbf{v}_v |C_l|^2
\end{aligned}$$

Appendix G

Dynamic σ Calculation

The algorithm for dynamically updating the σ parameter outlined in Gossel, 18³ is provided below.

1. Set an initial width parameter ($\sigma_v^{(I)}(t - dt)$) and a constant we will name D .
2. Calculate a cutoff distance via: $r_{cut}(t) = D\sigma_v^{(I)}(t - dt)$.
3. For each atom index, v , and replica, I , gather replicas within a cutoff distance of the current replica. Set the number of replicas within the cutoff distance to N .
4. Calculate the distance between atoms on different replicas.
5. Find the standard deviation of these distances and set the width of the gaussian, centered on atom v and replica I , to this standard deviation.
6. If the standard deviation is smaller than $\frac{D}{N} \min_I [\sigma_v^{(I)}(t - dt)]$ then set $\sigma_v^{(I)}(t) = \frac{D}{N} \min_I [\sigma_v^{(I)}(t - dt)]$.

Appendix H

Basis Transformation

We can expand the Schrödinger equation in terms of a diabatic basis, ϕ rather than an adiabatic one, ψ . These 2 expansions are given in equations (H.1) and (H.2).

$$|\Psi\rangle = \sum_n C_n |\psi_n\rangle \quad (\text{H.1})$$

$$|\Psi\rangle = \sum_l u_l |\phi_l\rangle \quad (\text{H.2})$$

It follows from this we can define a transformation matrix, U_{ln} to transform between the adiabatic and diabatic bases. This is shown in equation (H.3) where the $\overset{\leftrightarrow}{I}$ symbol represents the identity matrix. This identity only holds in the orthogonal diabatic basis ϕ and wouldn't hold for non-orthogonal bases.

$$|\psi_n\rangle = \overset{\leftrightarrow}{I} |\psi_n\rangle = \sum_l |\phi_l\rangle \langle \phi_l| \psi_n\rangle = \sum_l |\phi_l\rangle U_{ln} \quad (\text{H.3})$$

A similar relation between expansion coefficients exists

$$\sum_n C_n |\psi_n\rangle = \sum_l u_l |\phi_l\rangle \quad (\text{H.4})$$

$$\sum_n C_n \langle \psi_m | \psi_n \rangle = \sum_l u_l \langle \psi_m | \phi_l \rangle \quad (\text{H.5})$$

$$C_m = \sum_l u_l U_{lm}^* \quad (\text{H.6})$$

Finally an important property of the transformation matrix is given in equation (H.7).

$$\sum_m U_{im} U_{lm}^* = \sum_m \langle \phi_i | \psi_m \rangle \langle \psi_m | \phi_l \rangle = \langle \phi_i | \phi_l \rangle = \delta_{il} \quad (\text{H.7})$$

Equations (H.3), (H.6) and (H.7) will be used below to transform the propagation equations from the adiabatic basis to the diabatic one.

H.1 Forces

The equation for the propagation of the forces in the adiabatic basis is:

$$\begin{aligned} \mathbf{F}_v^{(I)} = & - \sum_n |C_n^{(I)}|^2 \nabla_v E_n^{(I)} - \sum_{n,m} C_m^{*(I)} C_n^{(I)} \left(E_n^{(I)} - E_m^{(I)} \right) \mathbf{d}_{v,mn}^{ad,(I)} \\ & - \sum_{m,n} |C_m^{(I)}|^2 \left(\sum_{v'}^{N_n} \frac{2}{\hbar M_{v'}} \mathcal{Q}_{v',mn}^{(I)} \cdot \mathbf{f}_{m,v'}^{(I)} \right) [\mathbf{f}_{n,v}^{(I)} - \mathbf{f}_{m,v}^{(I)}] |C_n^{(I)}|^2 \end{aligned} \quad (\text{H.8})$$

The quantum momentum part of the equation cannot be easily transformed so this will focus on the Ehrenfest part:

$$\mathbf{F}_{eh,v}^{(I)} = - \sum_n |C_n^{(I)}|^2 \nabla_v E_n^{(I)} - \sum_{n,m} C_m^{*(I)} C_n^{(I)} \left(E_n^{(I)} - E_m^{(I)} \right) \mathbf{d}_{v,mn}^{ad,(I)} \quad (\text{H.9})$$

Using equation (10) in Carof, 17⁶⁸ and the Hellman-Feynman theorem we can rewrite equation (H.9) as equation (H.10):

$$\mathbf{F}_{eh,v}^{(I)} = \sum_{m,n} C_m^{*(I)} C_n^{(I)} \langle \psi_m | \nabla_v H | \psi_n \rangle \quad (\text{H.10})$$

We can substitute the coefficients and basis functions for those in equations (H.3) and (H.6). This carried out in equation (H.15). However, I have removed the trajectory and

atom index from the terms to make the notation clearer.

$$F_{eh,v} = \sum_{m,n} C_m^* C_n \langle \psi_m | \nabla H | \psi_n \rangle \quad (\text{H.11})$$

$$= \sum_{m,n} \sum_i u_i^* U_{im} \sum_j u_j U_{jn}^* \sum_l U_{lm}^* \sum_k U_{kn} \langle \phi_l | \nabla H | \phi_k \rangle \quad (\text{H.12})$$

$$= \sum_{m,n} \sum_{i,j,k,l} u_i^* u_j U_{im} U_{lm}^* U_{jn}^* U_{kn} \langle \phi_l | \nabla H | \phi_k \rangle \quad (\text{H.13})$$

$$= \sum_{i,j,k,l} u_i^* u_j \delta_{il} \delta_{jk} \langle \phi_l | \nabla H | \phi_k \rangle \quad (\text{H.14})$$

$$= \sum_{i,j} u_i^* u_j \langle \phi_i | \nabla H | \phi_j \rangle \quad (\text{H.15})$$

However, in the code the expectation value of the gradient of the Hamiltonian ($\langle \phi_i | \nabla H | \phi_j \rangle$) isn't very easily calculable. However, the gradient of the Hamiltonian matrix elements ($\nabla \langle \phi_i | H | \phi_j \rangle$) is easily calculable via the overlap term, $\nabla H = C \nabla S_{ij}$. Therefore, using chain rule we can re-write equation (H.15) as:

$$F_{eh,v} = \sum_{i,j} u_i^* u_j \langle \phi_i | \nabla H | \phi_j \rangle \quad (\text{H.16})$$

$$= \sum_{i,j} u_i^* u_j (\nabla \langle \phi_i | H | \phi_j \rangle - \langle \nabla \phi_i | H | \phi_j \rangle - \langle \phi_i | H | \nabla \phi_j \rangle) \quad (\text{H.17})$$

$$= \sum_{i,j} u_i^* u_j \left(\nabla \langle \phi_i | H | \phi_j \rangle - \sum_l \langle \nabla \phi_i | \phi_l \rangle \langle \phi_l | H | \phi_j \rangle - \sum_l \langle \phi_i | H | \phi_l \rangle \langle \phi_l | \nabla \phi_j \rangle \right) \quad (\text{H.18})$$

$$= \sum_{i,j} u_i^* u_j \left(\nabla \langle \phi_i | H | \phi_j \rangle + \sum_l \mathbf{d}_{il} \langle \phi_l | H | \phi_j \rangle - \sum_l \mathbf{d}_{lj} \langle \phi_i | H | \phi_l \rangle \right) \quad (\text{H.19})$$

Giving the final equation for the transformed forces as:

$$\mathbf{F}_{eh,v}^{(I)} = \sum_{i,j} \mathbf{u}_i^{*(I)} \mathbf{u}_j^{(I)} \left(\nabla_v H_{ij}^{(I)} + \sum_l \mathbf{d}_{lk,v}^{(I)} H_{lj}^{(I)} - \sum_l \mathbf{d}_{lj,v}^{(I)} H_{il} \right) \quad (\text{H.20})$$

Appendix I

Adiabatic State Initialisation

By diagonalising the Hamiltonian we get the adiabatic energies (eigenvalues) for each state and transformation matrix (eigenvectors) to calculate diabatic states \mathbb{U} . We can calculate diabatic coefficients corresponding to each adiabatic state via equation (I.1) below.

$$\mathbb{U}\mathbf{C}_n = \mathbf{u}_n \quad (\text{I.1})$$

Where \mathbb{U} is the transformation matrix of size $(N_{\text{mol}}, N_{\text{mol}})$, \mathbf{C} is a complex vector of size N_{mol} containing coefficients for adiabatic state n and \mathbf{u} is a complex vector of size N_{mol} containing coefficients for diabatic state n .

Seeing as we would like to find the diabatic population corresponding to each adiabatic state we localise coefficients on each pure adiabatic state and carry out the transformation e.g: $C_i = (1+0i, 0+0i, 0+0i, \dots)$ when we want to find the diabatic coefficient corresponding to state 1 and $C_i = (0+0i, 1+0i, 0+0i, \dots)$ when we want to find the diabatic coefficient corresponding to state 2 etc.. Therefore, the column, n , of the transformation matrix, \mathbb{U} , gives the diabatic coefficients corresponding to adiabatic state, n , as shown below in equation (I.2)

$$U_{in} = u_i \quad (\text{I.2})$$

Where n is the adiabatic state index and i is the diabatic (molecular) state index.

Once we have the diabatic state corresponding to each adiabatic state, and the en-

ergy of that adiabatic state, we can find which state best fulfills the requirements of being close to the center of the system and being within 3KT of the ground state. In order to do this, we can loop over each adiabatic state in increasing order of energy. The center of the system is calculated and the population weighted average center of mass, \mathbf{R}_n of the diabatic coefficients corresponding to adiabatic state n is calculated as in equation (I.3).

$$\mathbf{R}_n = \sum_i |u_i|^2 \mathbf{R}_{COM,i} \quad (\text{I.3})$$

The Euclidean distance between the center of the system and $\mathbf{R}_{COM,i}$ is calculated and if this distance is below some threshold value then we initialise the surface hopping trajectory on that adiabatic state. If we do not find any states within 3KT of the ground state and within an acceptable radius of the center we start again this time increasing the maximum allowed distance from the center. If this maximum allowed distance is increased such that we reach another threshold distance the energy threshold is increased this time until a state is found that is close enough to the center. In this way we find an adiabatic state, which when transformed, gives a diabatic population close to center of the system and near the ground state energy.

Appendix J

Analytic Overlap Method

Appendix K

Colophon

This is a description of the tools you used to make your thesis. It helps people make future documents, reminds you, and looks good.

(example) This document was set in the Times Roman typeface using L^AT_EX (specifically LuaTeX) and BibTeX, composed with Vim Used Archer, Kathleen etc...

Bibliography

- [1] Federica Agostini, Ali Abedi, Yasumitsu Suzuki, Seung Kyu Min, Neepa T. Maitra, and E. K. U. Gross. The exact forces on classical nuclei in non-adiabatic charge transfer. *The Journal of Chemical Physics*, 142(8):084303, February 2015.
- [2] Federica Agostini, Seung Kyu Min, Ali Abedi, and E. K. U. Gross. Quantum-Classical Nonadiabatic Dynamics: Coupled- vs Independent-Trajectory Methods. *Journal of Chemical Theory and Computation*, 12(5):2127–2143, May 2016.
- [3] Graeme H. Gossel, Federica Agostini, and Neepa T. Maitra. Coupled-Trajectory Mixed Quantum-Classical Algorithm: A Deconstruction. *Journal of Chemical Theory and Computation*, August 2018.
- [4] William Humphrey, Andrew Dalke, and Klaus Schulten. VMD – Visual Molecular Dynamics. *Journal of Molecular Graphics*, 14:33–38, 1996.
- [5] John Stone. An Efficient Library for Parallel Ray Tracing and Animation. Master’s thesis, Computer Science Department, University of Missouri-Rolla, April 1998.
- [6] C. K. Chiang, C. R. Fincher, Y. W. Park, A. J. Heeger, H. Shirakawa, E. J. Louis, S. C. Gau, and Alan G. MacDiarmid. Electrical Conductivity in Doped Polyacetylene. *Physical Review Letters*, 39(17):1098–1101, October 1977.
- [7] Hideki Shirakawa, Edwin J. Louis, Alan G. MacDiarmid, Chwan K. Chiang, and Alan J. Heeger. Synthesis of electrically conducting organic polymers: halogen derivatives of polyacetylene, $(CH)_x$. *J. Chem. Soc., Chem. Commun.*, 0(16):578–580, Jan 1977.

- [8] Bernard Kippelen and Jean-Luc Brédas. Organic photovoltaics. *Energy Environ. Sci.*, 2(3):251–261, 2009.
- [9] M. J. Małachowski and J. Żmija. Organic field-effect transistors. *Opto-Electron. Rev.*, 18(2):121–136, Jun 2010.
- [10] N. Thejo Kalyani and S. J. Dhoble. Organic light emitting diodes: Energy saving lighting technology—A review. *Renewable Sustainable Energy Rev.*, 16(5):2696–2723, Jun 2012.
- [11] Sebastian Reineke, Frank Lindner, Gregor Schwartz, Nico Seidler, Karsten Walzer, Björn Lüssem, and Karl Leo. White organic light-emitting diodes with fluorescent tube efficiency. *Nature*, 459(7244):234, May 2009.
- [12] Kazuki Kato, Toshihiko Iwasaki, and Takatoshi Tsujimura. Over 130 lm/w all-phosphorescent white oleds for next-generation lighting. *Journal of Photopolymer Science and Technology*, 28:335–340, 10 2015.
- [13] Veaceslav Coropceanu, Jérôme Cornil, Demetrio A. da Silva Filho, Yoann Olivier, Robert Silbey, and Jean-Luc Brédas. Charge Transport in Organic Semiconductors. *Chemical Reviews*, 107(4):926–952, April 2007.
- [14] Samuele Giannini, Antoine Carof, Matthew Ellis, Hui Yang, Orestis George Ziogos, Soumya Ghosh, and Jochen Blumberger. Quantum localization and delocalization of charge carriers in organic semiconducting crystals. *Nature Communications*, 10(1):3843, Aug 2019.
- [15] Alessandro Troisi. Charge transport in high mobility molecular semiconductors: classical models and new theories. *Chem. Soc. Rev.*, 40:2347–2358, 2011.
- [16] Simone Fratini, Didier Mayou, and Sergio Ciuchi. The transient localization scenario for charge transport in crystalline organic materials. *Advanced Functional Materials*, 26(14):2292–2315, 2016.

- [17] I. Yavuz. Dichotomy between the band and hopping transport in organic crystals: insights from experiments. *Physical Chemistry Chemical Physics*, 19(38):25819–25828, 2017.
- [18] J. S. Brown and S. E. Shaheen. Introducing correlations into carrier transport simulations of disordered materials through seeded nucleation: impact on density of states, carrier mobility, and carrier statistics. *J. Phys.: Condens. Matter*, 30(13):135702, Mar 2018.
- [19] Tino Zimmerling and Bertram Batlogg. Improving charge injection in high-mobility rubrene crystals: From contact-limited to channel-dominated transistors. *Journal of Applied Physics*, 115(16):164511, 2014.
- [20] V. Podzorov, E. Menard, A. Borissov, V. Kiryukhin, J. A. Rogers, and M. E. Gershenson. Intrinsic charge transport on the surface of organic semiconductors. *Phys. Rev. Lett.*, 93:086602, Aug 2004.
- [21] Samuele Giannini, Antoine Carof, and Jochen Blumberger. Crossover from Hopping to Band-Like Charge Transport in an Organic Semiconductor Model: Atomistic Nonadiabatic Molecular Dynamics Simulation. *The Journal of Physical Chemistry Letters*, 9(11):3116–3123, June 2018.
- [22] Harald Oberhofer, Karsten Reuter, and Jochen Blumberger. Charge Transport in Molecular Materials: An Assessment of Computational Methods. *Chemical Reviews*, 117(15):10319–10357, August 2017.
- [23] John C. Tully. Nonadiabatic Dynamics. pages 34–71.
- [24] Simone Pisana, Michele Lazzeri, Cinzia Casiraghi, Kostya S. Novoselov, A. K. Geim, Andrea C. Ferrari, and Francesco Mauri. Breakdown of the adiabatic Born–Oppenheimer approximation in graphene. *Nat. Mater.*, 6(3):198, Feb 2007.
- [25] M. Born and R. Oppenheimer. Zur Quantentheorie der Moleküle. *Ann. Phys.*, 389(20):457–484, Jan 1927.

- [26] Sharon Hammes-Schiffer. Theoretical Perspectives on Proton-Coupled Electron Transfer Reactions. *Acc. Chem. Res.*, 34(4):273–281, Apr 2001.
- [27] Sharon Hammes-Schiffer and John C. Tully. Proton transfer in solution: Molecular dynamics with quantum transitions. *J. Chem. Phys.*, 101(6):4657–4667, Sep 1994.
- [28] My Hang V. Huynh and Thomas J. Meyer. Proton-coupled electron transfer. *Chemical Reviews*, 107(11):5004–5064, Nov 2007.
- [29] John C. Tully. Nonadiabatic molecular dynamics. *International Journal of Quantum Chemistry*, 40(S25):299–309, 1991.
- [30] Raymond Kapral and Giovanni Ciccotti. Mixed quantum-classical dynamics. *J. Chem. Phys.*, 110(18):8919–8929, May 1999.
- [31] Todd J. Martínez*. Insights for Light-Driven Molecular Devices from Ab Initio Multiple Spawning Excited-State Dynamics of Organic and Biological Chromophores. American Chemical Society, Oct 2005.
- [32] Guillermo Albareda, Heiko Appel, Ignacio Franco, Ali Abedi, and Angel Rubio. Correlated Electron-Nuclear Dynamics with Conditional Wave Functions. *Phys. Rev. Lett.*, 113(8):083003, Aug 2014.
- [33] John C. Tully. Molecular dynamics with electronic transitions. *J. Chem. Phys.*, 93(2):1061–1071, Jul 1990.
- [34] R. L et al Whetten. Molecular dynamics beyond the adiabatic approximation: New experiments and theory. *Ann. Rev. Phys. Chem.*, 36:277–320.
- [35] Neil Shenvi, Joseph E. Subotnik, and Weitao Yang. Simultaneous-trajectory surface hopping: A parameter-free algorithm for implementing decoherence in nonadiabatic dynamics. *J. Chem. Phys.*, 134(14):144102, Apr 2011.
- [36] D. F. Coker and L. Xiao. Methods for molecular dynamics with nonadiabatic transitions. *J. Chem. Phys.*, 102(1):496–510, Jan 1995.

- [37] Joseph E. Subotnik, Amber Jain, Brian Landry, Andrew Petit, Wenjun Ouyang, and Nicole Bellonzi. Understanding the surface hopping view of electronic transitions and decoherence. *Annual Review of Physical Chemistry*, 67(1):387–417, 2016. PMID: 27215818.
- [38] Giovanni Granucci, Maurizio Persico, and Alberto Zoccante. Including quantum decoherence in surface hopping. *The Journal of Chemical Physics*, 133(13):134111, 2010.
- [39] Heather M. Jaeger, Sean Fischer, and Oleg V. Prezhdo. Decoherence-induced surface hopping. *The Journal of Chemical Physics*, 137(22):22A545, 2012.
- [40] Amber Jain, Ethan Alguire, and Joseph E. Subotnik. An efficient, augmented surface hopping algorithm that includes decoherence for use in large-scale simulations. *Journal of Chemical Theory and Computation*, 12(11):5256–5268, Nov 2016.
- [41] Joseph E. Subotnik and Neil Shenvi. A new approach to decoherence and momentum rescaling in the surface hopping algorithm. *The Journal of Chemical Physics*, 134(2):024105, 2011.
- [42] Xiaosong Li, John C. Tully, H. Bernhard Schlegel, and Michael J. Frisch. Ab initio Ehrenfest dynamics. *J. Chem. Phys.*, 123(8):084106, Aug 2005.
- [43] Kenichiro Saita and Dmitrii V. Shalashilin. On-the-fly ab initio molecular dynamics with multiconfigurational Ehrenfest method. *J. Chem. Phys.*, 137(22):22A506, Dec 2012.
- [44] Daniela Kohen, Frank H. Stillinger, and John C. Tully. Model studies of nonadiabatic dynamics. *J. Chem. Phys.*, 109(12):4713–4725, Sep 1998.
- [45] John C. Tully. Perspective: Nonadiabatic dynamics theory. *The Journal of Chemical Physics*, 137(22):22A301, December 2012.
- [46] Priya V. Parandekar and John C. Tully. Detailed Balance in Ehrenfest Mixed Quantum-Classical Dynamics. *Journal of Chemical Theory and Computation*, 2(2):229–235, March 2006.

- [47] Ali Abedi, Neepa T. Maitra, and E. K. U. Gross. Exact Factorization of the Time-Dependent Electron-Nuclear Wave Function. *Physical Review Letters*, 105(12), September 2010.
- [48] Federica Agostini, Seung Kyu Min, and E. K. U. Gross. Semiclassical analysis of the electron-nuclear coupling in electronic non-adiabatic processes. *Annalen der Physik*, 527(9-10):546–555, October 2015.
- [49] Federica Agostini, Ali Abedi, Yasumitsu Suzuki, and E.K.U. Gross. Mixed quantum-classical dynamics on the exact time-dependent potential energy surface: a fresh look at non-adiabatic processes. *Molecular Physics*, 111(22-23):3625–3640, December 2013.
- [50] Ali Abedi, Federica Agostini, Yasumitsu Suzuki, and E. K. U. Gross. Dynamical Steps that Bridge Piecewise Adiabatic Shapes in the Exact Time-Dependent Potential Energy Surface. *Physical Review Letters*, 110(26), June 2013.
- [51] Seung Kyu Min, Ali Abedi, Kwang S. Kim, and E. K. U. Gross. Is the Molecular Berry Phase an Artifact of the Born-Oppenheimer Approximation? *Phys. Rev. Lett.*, 113(26):263004, Dec 2014.
- [52] Farnaz A. Shakib and Pengfei Huo. Ring Polymer Surface Hopping: Incorporating Nuclear Quantum Effects into Nonadiabatic Molecular Dynamics Simulations. *J. Phys. Chem. Lett.*, 8(13):3073–3080, Jul 2017.
- [53] Basile F. E. Curchod, Ivano Tavernelli, and Ursula Rothlisberger. Trajectory-based solution of the nonadiabatic quantum dynamics equations: an on-the-fly approach for molecular dynamics simulations. *PCCP*, 13(8):3231–3236, Feb 2011.
- [54] Ivano Tavernelli. Ab initio–driven trajectory-based nuclear quantum dynamics in phase space. *Phys. Rev. A*, 87(4):042501, Apr 2013.
- [55] Arne Scherrer, Federica Agostini, Daniel Sebastiani, E. K. U. Gross, and Rodolphe Vuilleumier. Nuclear velocity perturbation theory for vibrational circular dichroism:

- An approach based on the exact factorization of the electron-nuclear wave function. *J. Chem. Phys.*, 143(7):074106, Aug 2015.
- [56] Seung Kyu Min, Federica Agostini, Ivano Tavernelli, and E. K. U. Gross. Ab Initio Nonadiabatic Dynamics with Coupled Trajectories: A Rigorous Approach to Quantum (De)Coherence. *The Journal of Physical Chemistry Letters*, 8(13):3048–3055, July 2017.
- [57] John C. Tully. Molecular dynamics with electronic transitions. *The Journal of Chemical Physics*, 93(2):1061–1071, July 1990.
- [58] Fruzsina Gajdos, Siim Valner, Felix Hoffmann, Jacob Spencer, Marian Breuer, Adam Kubas, Michel Dupuis, and Jochen Blumberger. Ultrafast Estimation of Electronic Couplings for Electron Transfer between -Conjugated Organic Molecules. *Journal of Chemical Theory and Computation*, 10(10):4653–4660, October 2014.
- [59] J. VandeVondele, J; Hutter. Gaussian basis sets for accurate calculations on molecular systems in gas and condensed phases. *The Journal of Chemical Physics*, 127(11).
- [60] J. Spencer, F. Gajdos, and J. Blumberger. FOB-SH: Fragment orbital-based surface hopping for charge carrier transport in organic and biological molecules and materials. *The Journal of Chemical Physics*, 145(6):064102, August 2016.
- [61] Steven L. Fiedler and Jussi Eloranta. Nonadiabatic dynamics by mean-field and surface-hopping approaches: energy conservation considerations. *Molecular Physics*, 108(11):1471–1479, 2010.
- [62] Joseph E. Subotnik. Augmented ehrenfest dynamics yields a rate for surface hopping. *The Journal of Chemical Physics*, 132(13):134112, 2010.
- [63] R.B. Leighton Richard P. Feynman. *The Feynman Lectures on Physics*, Vol 3. Addison–Wesley, 1998.
- [64] James Kirkpatrick. An approximate method for calculating transfer integrals based on the zindo hamiltonian. *International Journal of Quantum Chemistry*, 108(1):51–56, 2008.

- [65] Harald Oberhofer and Jochen Blumberger. Revisiting electronic couplings and incoherent hopping models for electron transport in crystalline c60 at ambient temperatures. *Phys. Chem. Chem. Phys.*, 14:13846–13852, 2012.
- [66] Alessandro Troisi and Giorgio Orlandi. Hole migration in dna: a theoretical analysis of the role of structural fluctuations. *The Journal of Physical Chemistry B*, 106(8):2093–2101, Feb 2002.
- [67] Adam Kubas, Felix Hoffmann, Alexander Heck, Harald Oberhofer, Marcus Elstner, and Jochen Blumberger. Electronic couplings for molecular charge transfer: Benchmarking cdft, fodft, and fodftb against high-level ab initio calculations. *The Journal of Chemical Physics*, 140(10):104105, 2014.
- [68] Antoine Carof, Samuele Giannini, and Jochen Blumberger. Detailed balance, internal consistency, and energy conservation in fragment orbital-based surface hopping. *The Journal of Chemical Physics*, 147(21):214113, December 2017.
- [69] Antoine Carof, Samuele Giannini, and Jochen Blumberger. Detailed balance, internal consistency, and energy conservation in fragment orbital-based surface hopping. *The Journal of Chemical Physics*, 147(21):214113, 2017.
- [70] Soumya Ghosh, Samuele Giannini, Kevin Lively, and Jochen Blumberger. Nonadiabatic dynamics with quantum nuclei: simulating charge transfer with ring polymer surface hopping. *Faraday Discuss.*, 221:501–525, 2020.
- [71] Antoine Carof, Samuele Giannini, and Jochen Blumberger. How to calculate charge mobility in molecular materials from surface hopping non-adiabatic molecular dynamics – beyond the hopping/band paradigm. *Phys. Chem. Chem. Phys.*, 21:26368–26386, 2019.
- [72] J. Spencer, F. Gajdos, and J. Blumberger. Fob-sh: Fragment orbital-based surface hopping for charge carrier transport in organic and biological molecules and materials. *The Journal of Chemical Physics*, 145(6):064102, 2016.

- [73] Jacob Spencer, Laura Scalfi, Antoine Carof, and Jochen Blumberger. Confronting surface hopping molecular dynamics with marcus theory for a molecular donor–acceptor system. *Faraday Discuss.*, 195:215–236, 2016.
- [74] Samuele Giannini, Orestis George Ziogos, Antoine Carof, Matthew Ellis, and Jochen Blumberger. Flickering polarons extending over ten nanometres mediate charge transport in high-mobility organic crystals. *Advanced Theory and Simulations*, 3(9):2000093, 2020.
- [75] Samuele Giannini, Antoine Carof, and Jochen Blumberger. Crossover from hopping to band-like charge transport in an organic semiconductor model: Atomistic nonadiabatic molecular dynamics simulation. *The Journal of Physical Chemistry Letters*, 9(11):3116–3123, Jun 2018.
- [76] Orestis George Ziogos, Samuele Giannini, Matthew Ellis, and Jochen Blumberger. Identifying high-mobility tetracene derivatives using a non-adiabatic molecular dynamics approach. *J. Mater. Chem. C*, 8:1054–1064, 2020.
- [77] Fruzsina Gajdos, Siim Valner, Felix Hoffmann, Jacob Spencer, Marian Breuer, Adam Kubas, Michel Dupuis, and Jochen Blumberger. Ultrafast estimation of electronic couplings for electron transfer between π -conjugated organic molecules. *Journal of Chemical Theory and Computation*, 10(10):4653–4660, Oct 2014.
- [78] Adam Kubas, Fruzsina Gajdos, Alexander Heck, Harald Oberhofer, Marcus Elstner, and Jochen Blumberger. Electronic couplings for molecular charge transfer: benchmarking cdft, fodft and fodftb against high-level ab initio calculations. ii. *Phys. Chem. Chem. Phys.*, 17:14342–14354, 2015.
- [79] Biswajit Ray, Aditya G. Baradwaj, Bryan W. Boudouris, and Muhammad A. Alam. Defect characterization in organic semiconductors by forward bias capacitance–voltage (fb-cv) analysis. *The Journal of Physical Chemistry C*, 118(31):17461–17466, Aug 2014.
- [80] W. S. Hu, Y. T. Tao, Y. J. Hsu, D. H. Wei, and Y. S. Wu. Molecular orientation of

- evaporated pentacene films on gold: alignment effect of self-assembled monolayer. *Langmuir*, 21(6):2260–2266, Mar 2005.
- [81] Tatsuo Hasegawa and Jun Takeya. Organic field-effect transistors using single crystals. *Science and Technology of Advanced Materials*, 10(2):024314, 2009.
- [82] John E. Anthony, James S. Brooks, David L. Eaton, and Sean R. Parkin. Functionalized pentacene: improved electronic properties from control of solid-state order. *Journal of the American Chemical Society*, 123(38):9482–9483, Sep 2001.
- [83] John E. Anthony, David L. Eaton, and Sean R. Parkin. A road map to stable, soluble, easily crystallized pentacene derivatives. *Organic Letters*, 4(1):15–18, Jan 2002.
- [84] A. D’Angelo, B. Edgar, A. P. Hurt, and M. D. Antonijević. Physico-chemical characterisation of three-component co-amorphous systems generated by a melt-quench method. *Journal of Thermal Analysis and Calorimetry*, 134(1):381–390, Oct 2018.
- [85] Wanderlā L. Scopel, Antônio J. R. da Silva, and A. Fazzio. Amorphous hfo_2 and $\text{hf}_{1-x}\text{si}_x\text{O}$ via a melt-and-quench scheme using ab initio molecular dynamics. *Phys. Rev. B*, 77:172101, May 2008.
- [86] Seth S. Berbano, Inseok Seo, Christian M. Bischoff, Katherine E. Schuller, and Steve W. Martin. Formation and structure of $\text{na}_2\text{s}+\text{p}_2\text{s}_5$ amorphous materials prepared by melt-quenching and mechanical milling. *Journal of Non-Crystalline Solids*, 358(1):93 – 98, 2012.
- [87] Pranav Karmwar, Kirsten Graeser, Keith C. Gordon, Clare J. Strachan, and Thomas Rades. Investigation of properties and recrystallisation behaviour of amorphous indomethacin samples prepared by different methods. *International Journal of Pharmaceutics*, 417(1):94 – 100, 2011. Advanced characterization techniques.
- [88] Min-Jin Ko, Joel Plawsky, and Meyer Birnboim. Fabrication of cds/ag hybrid quantum dot composites using a melt/quench method. *Journal of Non-Crystalline Solids*, 203:211 – 216, 1996. Optical and Electrical Propertias of Glasses.

- [89] Steve Plimpton. Fast parallel algorithms for short-range molecular dynamics. *Journal of Computational Physics*, 117(1):1 – 19, 1995.
- [90] Steve Plimpton. Lammps software. <http://lammps.sandia.gov>, 1995. [Online; accessed 21-Jan-2021].
- [91] Steve Plimpton, Roy Pollock, and Mark Stevens. Particle-mesh ewald and rRESPA for parallel molecular dynamics simulations. In In Proceedings of the Eighth SIAM Conference on Parallel Processing for Scientific Computing, 1997.
- [92] Christopher I. Bayly, Piotr Cieplak, C, and Peter A. Kollman. A well-behaved electrostatic potential based method using charge restraints for deriving atomic charges: the resp model. *The Journal of Physical Chemistry*, 97(40):10269–10280, Oct 1993.
- [93] M. J. Frisch, G. W. Trucks, H. B. Schlegel, G. E. Scuseria, M. A. Robb, J. R. Cheeseman, G. Scalmani, V. Barone, G. A. Petersson, H. Nakatsuji, X. Li, M. Caricato, A. V. Marenich, J. Bloino, B. G. Janesko, R. Gomperts, B. Mennucci, H. P. Hratchian, J. V. Ortiz, A. F. Izmaylov, J. L. Sonnenberg, D. Williams-Young, F. Ding, F. Lipparini, F. Egidi, J. Goings, B. Peng, A. Petrone, T. Henderson, D. Ranasinghe, V. G. Zakrzewski, J. Gao, N. Rega, G. Zheng, W. Liang, M. Hada, M. Ehara, K. Toyota, R. Fukuda, J. Hasegawa, M. Ishida, T. Nakajima, Y. Honda, O. Kitao, H. Nakai, T. Vreven, K. Throssell, J. A. Montgomery, Jr., J. E. Peralta, F. Ogliaro, M. J. Bearpark, J. J. Heyd, E. N. Brothers, K. N. Kudin, V. N. Staroverov, T. A. Keith, R. Kobayashi, J. Normand, K. Raghavachari, A. P. Rendell, J. C. Burant, S. S. Iyengar, J. Tomasi, M. Cossi, J. M. Millam, M. Klene, C. Adamo, R. Cammi, J. W. Ochterski, R. L. Martin, K. Morokuma, O. Farkas, J. B. Foresman, and D. J. Fox. Gaussian[®]16 Revision C.01, 2016. Gaussian Inc. Wallingford CT.
- [94] Junmei Wang, Romain M. Wolf, James W. Caldwell, Peter A. Kollman, and David A. Case. Development and testing of a general amber force field. *Journal of Computational Chemistry*, 25(9):1157–1174, 2004.

- [95] Makoto Yoneya, Masahiro Kawasaki, and Masahiko Ando. Molecular dynamics simulations of pentacene thin films: The effect of surface on polymorph selection. *J. Mater. Chem.*, 20:10397–10402, 2010.
- [96] Makoto Yoneya, Masahiro Kawasaki, and Masahiko Ando. Are pentacene monolayer and thin-film polymorphs really substrate-induced? a molecular dynamics simulation study. *The Journal of Physical Chemistry C*, 116(1):791–795, Jan 2012.
- [97] Makoto Yoneya. Simulation of crystallization of pentacene and its derivatives from solution. *The Journal of Physical Chemistry C*, Jan 2021.
- [98] Ryan A. Miller, Amanda Larson, and Karsten Pohl. Novel surface diffusion characteristics for a robust pentacene derivative on au(111) surfaces. *Chemical Physics Letters*, 678:28 – 34, 2017.
- [99] Dong Wang, Ling Tang, Mengqiu Long, and Zhigang Shuai. Anisotropic thermal transport in organic molecular crystals from nonequilibrium molecular dynamics simulations. *The Journal of Physical Chemistry C*, 115(13):5940–5946, Apr 2011.
- [100] Florian Steiner, Carl Poelking, Dorota Niedzialek, Denis Andrienko, and Jenny Nelson. Influence of orientation mismatch on charge transport across grain boundaries in tri-isopropylsilylethynyl (tips) pentacene thin films. *Phys. Chem. Chem. Phys.*, 19:10854–10862, 2017.
- [101] Ida Bagus Hendra Prastiawan, Jingxiang Xu, Yusuke Ootani, Yuji Higuchi, Nobuki Ozawa, Shingo Maruyama, Yuji Matsumoto, and Momoji Kubo. Molecular interactions between pentacene and imidazolium ionic liquids: A molecular dynamics study. *Chemistry Letters*, 47(9):1154–1157, 2018.
- [102] EPA DSSTox. Epa dsstox. <https://comptox.epa.gov/dashboard/DTXSID7059648>, 2021. [Online; accessed 25-Jan-2021].
- [103] Stefan Schiefer, Martin Huth, Alexander Dobrinevski, and Bert Nickel. Determination of the crystal structure of substrate-induced pentacene polymorphs

- in fiber structured thin films. *Journal of the American Chemical Society*, 129(34):10316–10317, Aug 2007.
- [104] Martin Ester, Hans-Peter Kriegel, Jörg Sander, and Xiaowei Xu. A density-based algorithm for discovering clusters in large spatial databases with noise. pages 226–231. AAAI Press, 1996.